Research Square

Preprints are preliminary reports that have not undergone peer review.
They should not be considered conclusive, used to inform clinical practice,
or referenced by the media as validated information.

Structure-Sensitive Characterization of Additively Manufactured IN718 Using Hybrid Ultrasonic SPC-I and XCT-Derived Porosity Features

Amir Nayebzadeh

amirnayebzadeh@arizona.edu

The University of Arizona

Shreyas Athreya

The Woodlands College Park High School

Tribikram Kundu

The University of Arizona

I-Tzu Huang

University of Arizona

I-Ting Ho

University of Arizona

Research Article

Keywords: Additive manufacturing, Hybrid linear/nonlinear ultrasonics, sideband peak counting, Porosity characterization, Porosity Index (PI)

Posted Date: August 27th, 2026

DOI: https://doi.org/10.21203/rs.3.rs-10670757/v1

License: This work is licensed under a Creative Commons Attribution 4.0 International License.
Read Full License

Additional Declarations: No competing interests reported.

Structure-Sensitive Characterization of Additively Manufactured IN718 Using Hybrid Ultrasonic SPC-I and XCT-Derived Porosity Features

Abstract

Additive manufacturing (AM) of nickel-based superalloys such as Inconel 718 (IN718) enables the fabrication of complex, high-performance components; however, process-induced porosity remains a critical challenge affecting fatigue resistance and structural reliability. Rapid and physically interpretable characterization of porosity-sensitive acoustic behavior is therefore essential for scalable nondestructive evaluation of AM materials. This study investigates the Sideband Peak Count Index (SPC-I), a hybrid ultrasonic metric, as a rapid screening indicator of porosity evolution in additively manufactured IN718. SPC-I is treated as a hybrid ultrasonic metric because it captures cumulative contributions from both linear wave propagation and nonlinear defect-induced wave interactions. Microfocus X-ray computed tomography (XCT) was used to quantify pore structure and spatial characteristics, including pore size, porosity volume fraction, pore size variability, sphericity, and nearest-neighbor spacing. To improve the interpretation of hybrid ultrasonic response, a physics-informed Porosity Index (PI) was introduced by integrating normalized XCT-derived descriptors with SPC-I within a unified structure-sensitive framework. Linear regression, principal component analysis (PCA), hierarchical clustering, cluster-wise regression, statistical validation, and exploratory machine-learning analysis were employed to investigate relationships between the hybrid ultrasonic response and porosity characteristics. The results demonstrate that SPC-I is governed primarily by pore size evolution, structure irregularity, pore size variability, and cumulative defect interaction mechanisms rather than by porosity volume fraction alone. PCA and clustering analyses identified three physically meaningful porosity regimes corresponding to transitions from isolated pore behavior to interaction-dominated and spatially clustered defect networks. Cluster-wise regression produced improved correlations compared to global regression, indicating that hybrid ultrasonic response evolves differently across structure-dependent defect interaction states. The proposed PI framework enhanced the interpretation of hybrid acoustic behavior by capturing the coupled effects of pore size, defect density, structure, and spatial interaction within a single descriptor. To the authors' knowledge, this is the first study to propose and validate an integrated XCT–SPC-I–PI framework for porosity characterization in additively manufactured IN718. The framework provides a scalable and physically interpretable pathway for rapid porosity-sensitive characterization, defect-state screening, and future structural health monitoring of AM metallic materials.

Keywords: Additive manufacturing; Hybrid linear/nonlinear ultrasonics; sideband peak counting; Porosity characterization; Porosity Index (PI).

1. Introduction

Additive manufacturing (AM) of metallic alloys has significantly expanded the design and manufacturing capabilities of modern engineering systems by enabling the fabrication of geometrically complex structures that are difficult or impossible to produce using conventional subtractive methods. Among AM materials, Inconel 718 (IN718) has received substantial attention because of its excellent high-temperature strength, corrosion resistance, and fatigue performance, making it particularly attractive for aerospace, energy, and high-performance structural applications [1]. However, additively manufactured IN718 components commonly contain process-induced defects, especially porosity generated by lack-of-fusion mechanisms, gas entrapment, unstable melt-pool dynamics, and keyhole formation[2–5] . These defects strongly influence crack initiation, fatigue resistance, and long-term structural reliability, often becoming the dominant factor controlling structural performance in AM superalloys [3,4].

Accurate characterization of porosity is therefore essential for process qualification, quality assurance, and structural integrity assessment in AM materials. X-ray computed tomography (XCT), one of the nondestructive evaluation (NDE) method, has become one of the most powerful techniques for nondestructive porosity characterization because it enables three-dimensional quantification of pore size, structure, spatial distribution, clustering behavior, and volume fraction [6–10]. In AM alloys, XCT is particularly valuable because internal defects are often highly heterogeneous and difficult to detect using conventional surface-based inspection methods. Nevertheless, XCT remains expensive, time-consuming, computationally intensive, and constrained by trade-offs among scan resolution, field of view, and specimen size [6–10]. These limitations reduce its practicality for rapid and scalable inspection of large AM component populations.

Ultrasonic testing offers an NDE attractive complementary alternative because it is rapid, portable, and scalable for industrial inspection. Conventional linear ultrasonic methods are highly effective for detecting large cracks and macroscopic discontinuities; however, their sensitivity to distributed microstructural degradation and early-stage porosity evolution is often limited. Nonlinear ultrasonic techniques, by contrast, exploit waveform distortion mechanisms such as harmonic generation, wave modulation, and nonlinear sideband formation that are extremely sensitive to microstructural evolution, stress-induced nonlinearity, and contact acoustic nonlinearity [11–14]. These nonlinear mechanisms become increasingly significant in porous AM materials because distributed defects generate localized stress concentration and nonlinear scattering behavior that strongly influence broadband acoustic response [13–16].

Nonlinear ultrasonic testing was employed to evaluate microdefect-sensitive acoustic responses in the AM specimens. Unlike conventional linear ultrasonic methods, which primarily rely on reflection and scattering from large discontinuities, nonlinear ultrasonic techniques exploit waveform distortion phenomena such as higher harmonic generation and frequency modulation that cause spectral sideband formation. These effects are extremely sensitive to distributed porosity, stress localization, local contact acoustic nonlinearity, and early-stage defect formation [11–15]. Among different ultrasonic techniques, the Sideband Peak Count Index (SPC-I) has recently emerged as a promising hybrid linear/nonlinear technique for characterizing distributed damage and evolving structural nonlinearity [17–23]. SPC-I quantifies the number and intensity

of nonlinearity-induced spectral sidebands, thereby capturing cumulative nonlinear activity rather than relying on a few higher harmonic peak amplitudes. Previous studies have demonstrated that SPC-I is sensitive to crack growth in material, welded-joint degradation, distributed defect evolution, and stress-state variation. AM porosity involves complex combinations of defect size, structure, and spatial distribution [24]. SPC-I provides the necessary tool for characterizing such defects in additively manufactured materials.

Recent investigations have demonstrated the growing applicability of nonlinear ultrasonics to additive manufacturing. Hybrid acoustic techniques have been used for monitoring porosity evolution in AM parts and for in-situ characterization of metal AM processes [24,25]. Furthermore, Ho et al. demonstrated the feasibility of integrating nonlinear acoustics with microfocus XCT for nondestructive evaluation of AM IN718 [6]. Despite these advances, the physical relationship between hybrid ultrasonic response and XCT-derived porosity descriptors remains insufficiently understood. In particular, it is still unclear which porosity characteristics most strongly influence SPC-I behavior, how defect structure and spatial interaction influence hybrid response evolution, and whether structure-informed statistical frameworks can improve interpretation consistency across different porosity regimes [6,14,19–21,24,25]

A major challenge in interpreting nonlinear ultrasonic measurements in AM materials is that porosity cannot be fully represented by a single descriptor, such as pore volume fraction alone. Defect size, structure, variability, clustering behavior, and inter-defect spacing collectively influence local stress concentration, nonlinear scattering, and cumulative defect interaction [13–16]. Consequently, specimens exhibiting similar porosity fractions may still produce substantially different hybrid ultrasonic responses depending on the underlying defect topology and interaction state. This complexity motivates the need for a more physics-informed framework capable of relating hybrid ultrasonic response to evolving porosity interaction mechanisms rather than to isolated descriptors alone.

To address these challenges, the present study integrates XCT-derived porosity characterization, nonlinear ultrasonic SPC-I measurements, physics-informed feature construction, dimensionality reduction, and unsupervised clustering analysis to investigate porosity-sensitive hybrid behavior in additively manufactured IN718. A physics-informed Porosity Index (PI) is introduced to represent the combined influence of pore size, defect density, structure, spatial variability, and inter-defect interaction within a unified framework. The PI formulation is inspired by physics-based damage-index concepts and is intended to improve the interpretation of hybrid ultrasonic response beyond conventional single-parameter correlations [14,15,26].

In addition to direct SPC-I–porosity correlations, principal component analysis (PCA), hierarchical clustering, and cluster-wise regression analysis are employed to identify structure-dependent porosity regimes and evaluate whether hybrid ultrasonic response evolves differently across distinct defect interaction states [27–29]. The underlying hypothesis is that SPC-I is governed not only by porosity quantity, but also by transitions in defect interaction behavior associated with evolving pore structure and spatial clustering. Specifically, the hybrid response is expected to evolve from weak isolated-pore scattering behavior toward stronger interaction-dominated nonlinear regimes characterized by pore coalescence, irregular structure, and distributed defect-network interactions.

The objectives of this study are therefore:

- to evaluate the sensitivity of SPC-I to pore structure, pore size distribution, spatial organization, and porosity fraction in additively manufactured IN718.
- to introduce a physics-informed Porosity Index (PI) capable of improving the interpretation of hybrid ultrasonic response by integrating multiple XCT-derived descriptors into a unified structure-sensitive framework.
- to investigate whether structure-informed clustering improves the consistency and interpretability of SPC-I–porosity relationships across different defect interaction regimes; and
- to assess the feasibility of using SPC-I as a rapid screening characterization indicator of porosity state in additively manufactured materials.

The primary contribution of this work is the establishment of an integrated XCT–SPC-I–PI framework linking hybrid ultrasonic response to physically meaningful porosity evolution mechanisms in additively manufactured IN718. Unlike previous studies that primarily correlated ultrasonic parameters with individual XCT descriptors, the proposed framework integrates physics-informed feature construction, unsupervised learning, and hybrid ultrasonic characterization into a unified interpretation methodology. The results demonstrate that SPC-I is sensitive not only to porosity severity but also to the underlying structure, variability, spatial organization, and interaction behavior of distributed defects. These findings support the potential of SPC-I as a scalable and defect-sensitive indicator for rapid material screening, porosity-state classification, and nondestructive characterization of additively manufactured materials.

The overall methodology adopted in this study is summarized in Figure 1. The framework integrates additive manufacturing-induced porosity characterization, XCT-derived structure descriptors, physics-informed Porosity Index (PI) construction, dimensionality reduction, clustering analysis, and nonlinear ultrasonic SPC-I correlation to establish a structure-sensitive interpretation of evolving defect interaction behavior.

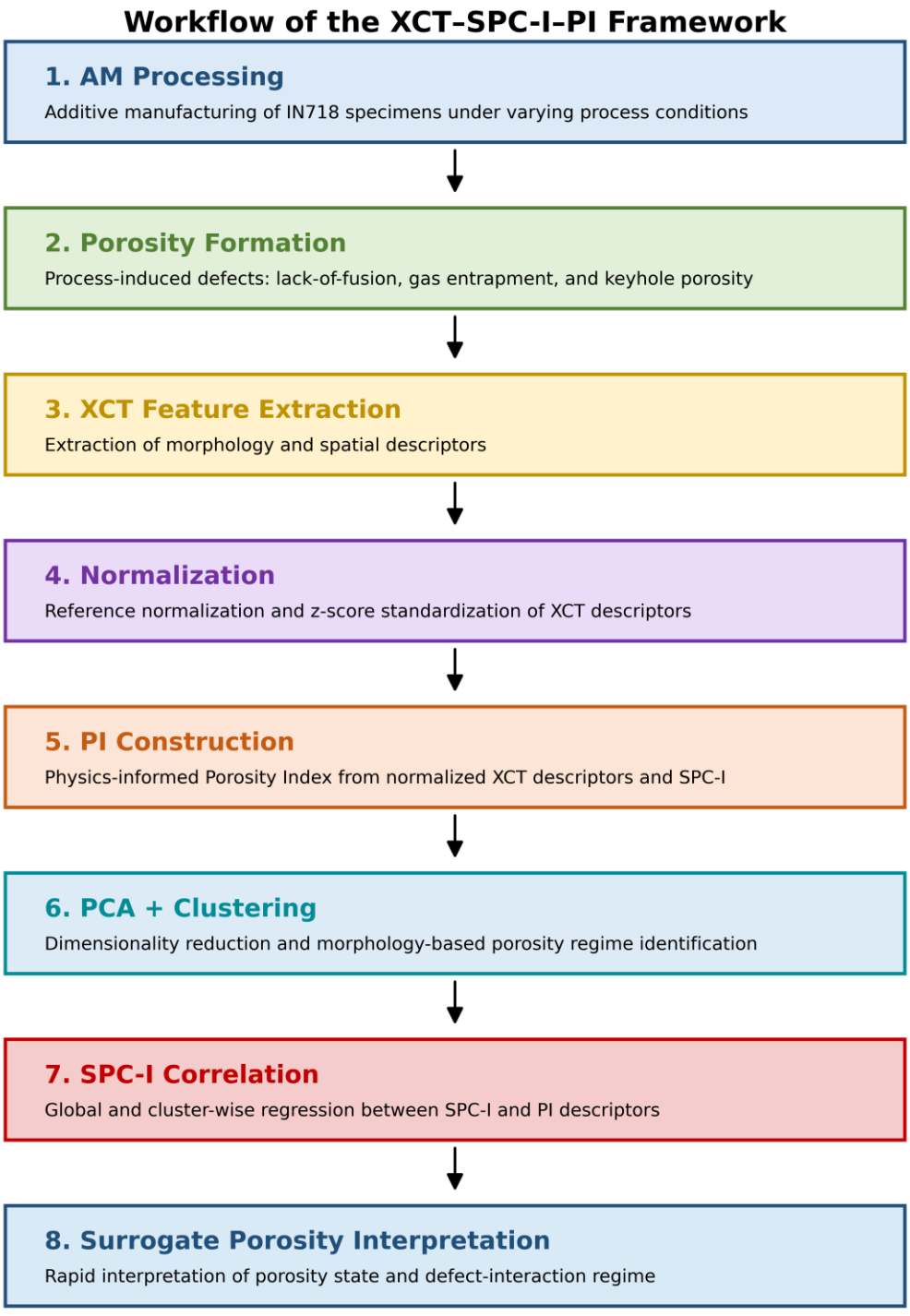

Figure 1. Integrated workflow of the proposed XCT–SPC-I–PI framework for structure-informed nonlinear ultrasonic characterization of porosity evolution in additively manufactured IN718.

2. Materials and Methods

2.1 Additive Manufacturing, Specimen Geometry, and XCT Procedure

The study was conducted on a set of twenty-nine additively manufactured (AM) Inconel 718 (IN718) specimens exhibiting varying levels of process-induced porosity. The AM specimens investigated in this study were fabricated using a laser powder bed fusion process (PBF-LB/M) with gas-atomized IN718 powder under an inert argon atmosphere to minimize oxidation and maintain process stability. Fabrication was conducted in collaboration with Lockheed Martin Corporation using a Velo3D Sapphire printer. Customized scan patterns generated using the embedded Flow 4.0 software were implemented to intentionally produce variations in pore size, volume fraction, structure, and spatial distribution. The processing parameters, including laser power, scan speed, laser spot size, hatch spacing, layer thickness, and scan strategy, were systematically adjusted to generate controlled variations in internal porosity. However, these detailed processing parameters are proprietary and therefore are not disclosed.

The dimensions of the AM specimens are schematically illustrated in Figure 2. The specimens were designed as cylindrical tensile bars with a reduced gauge section, with the build direction aligned along the longitudinal axis. The central gauge section, which served as the primary region of interest (ROI) for both XCT characterization and nonlinear ultrasonic testing, had a diameter of 6.10 mm and a length of 15.50 mm. The specimens were manufactured in near-net shape without subsequent post-processing machining to preserve the as-built microstructure and the original defect population generated during the AM process.

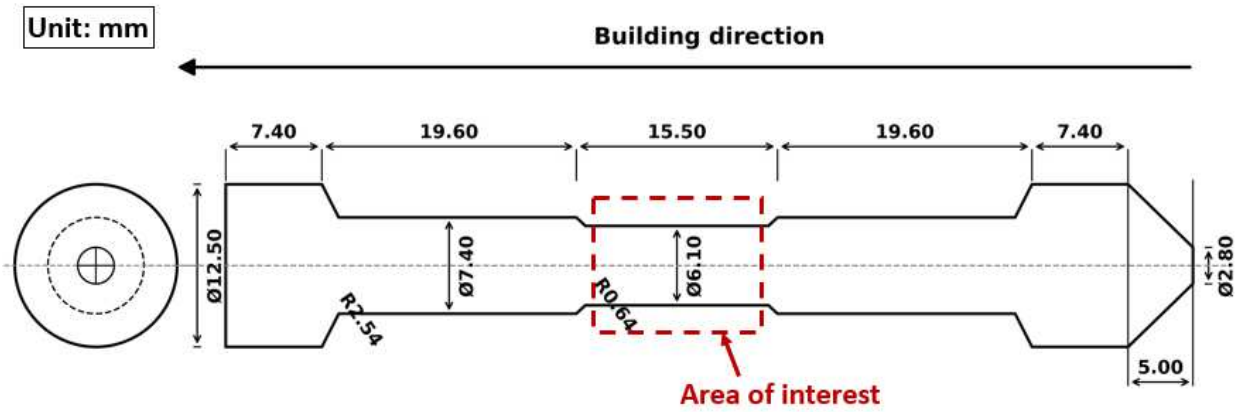

Figure 2. Schematic of the additively manufactured IN718 specimen geometry.

Microfocus X-ray computed tomography (μ-XCT) was employed to nondestructively characterize the internal structure of the specimens, with particular emphasis on pore structure, pore size distribution, and spatial defect organization within the gauge section (highlighted in Figure 2). [6–10] All scans were performed using a Shimadzu InspeXio SMX-225CT FPD HR Plus μ-XCT system, and the scanning parameters, including voltage, current, voxel size, and number of

projections, were optimized for the IN718 material system and specimen geometry, as shown in Table 1.

Table 1: XCT parameters used in the present investigation.

Parameters	Value
Voltage (kV)	160
Current (μA)	100
Source to object distance (mm)	26.5
Source to image distance (mm)	800
Acquisition rate (fps)	4.5
Voxel size (μm)	6
Number of views	3000

The acquired projection data were reconstructed into three-dimensional volumetric datasets, and standard reconstruction corrections, including beam-hardening compensation and signal normalization, were applied prior to analysis [6]. Visualization was performed using Paraview software [30,31]. Segmentation of the reconstructed volumes was performed using a threshold-based binarization procedure to distinguish solid material from void regions. A consistent iso-value threshold was applied to all specimens to ensure reproducibility and minimize segmentation variability across the dataset. Following segmentation, surface reconstruction techniques were employed to generate triangulated pore geometries using established computational geometry and alpha-shape reconstruction methods [32,33].

Individual pores were subsequently identified using connectivity-based algorithms, and quantitative descriptors were extracted to characterize pore structure, size evolution, and spatial interaction behavior. The extracted descriptors included maximum pore size, average pore size, porosity volume fraction, standard deviation (SD) of pore size, sphericity, standard deviation (SD) of sphericity, median nearest-neighbor distance, standard deviation (SD) of nearest-neighbor distance, epsilon (ε), and distance-at-epsilon metrics. Here, ε represents a spatial clustering parameter that characterizes the characteristic interaction distance between neighboring pores and is commonly used to quantify the degree of pore aggregation and defect-network formation within the material. The corresponding distance-at-epsilon descriptor represents the characteristic spatial scale associated with this clustering threshold. The standard deviation descriptors quantify the variability of pore size, pore shape, and pore spacing distributions, thereby providing measures of microstructural heterogeneity. Collectively, these descriptors were selected because they capture the dominant physical mechanisms expected to influence nonlinear ultrasonic behavior, including defect size evolution, structure irregularity, pore-density variation, spatial clustering, and inter-defect interaction effects [6,14,22,26,34,35].

The resulting XCT datasets provided detailed three-dimensional characterization of defect structure and distributed porosity interaction states within the AM specimens as shown in Figure 3. These structure-sensitive descriptors were subsequently used for normalization, physics-informed Porosity Index (PI) construction, principal component analysis (PCA), clustering

analysis, and cluster-wise nonlinear ultrasonic correlation analysis presented in the following sections.

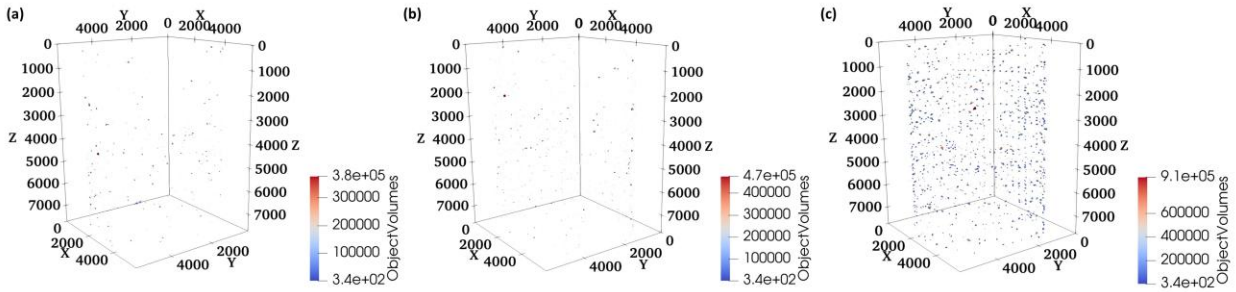

Figure 3. Examples of XCT visualization results. (a-c) represent samples 39B, 1B, and 12A, respectively.

2.2 Material System, Normalization, and XCT-Based Microstructural Characterization

To enable consistent comparison across specimens, all XCT-derived porosity descriptors and hybrid ultrasonic parameters were normalized with respect to a reference specimen (sample 49A). The normalization was defined as:

$$X_{i,\text{norm}} = \frac{X_i}{X_{i,\text{ref}}} \quad (1)$$

where X_i represents a given descriptor for specimen i, and $X_{i,\text{ref}}$ corresponds to the same descriptor measured for the reference specimen. This normalization framework emphasizes relative variations in pore structure, spatial organization, and hybrid response while reducing scale-dependent bias and improving comparability among specimens.

A comprehensive set of XCT-derived descriptors, as shown in Table 2, was extracted to characterize both morphological and spatial aspects of the pore population. These descriptors included maximum pore size, average pore size, porosity volume fraction, standard deviation of pore size, sphericity, standard deviation of sphericity, median nearest-neighbor distance, standard deviation of nearest-neighbor distance, epsilon, and distance-at-epsilon metrics. Collectively, these descriptors capture pore-size evolution, structure irregularity, spatial clustering behavior, and defect interaction characteristics that are expected to influence hybrid ultrasonic response mechanisms [6,9,14,17,22,26,34,35].

To investigate structure-dependent porosity regimes, principal component analysis (PCA) and unsupervised clustering methods were applied using the normalized XCT-derived descriptors. Prior to clustering, all descriptors were standardized to zero mean and unit variance to eliminate scale dependency among features. PCA was subsequently employed to reduce dimensionality and identify dominant modes of porosity variation within the dataset [27–29].

Hierarchical clustering using Ward linkage and K-means clustering were then applied to the reduced structure-sensitive feature space to identify groups of specimens exhibiting similar pore morphologies and spatial defect organization. Importantly, clustering was performed exclusively using XCT-derived descriptors without inclusion of SPC-I, allowing the hybrid ultrasonic response to be independently evaluated relative to the identified structure regimes. The clustering analysis was intended to determine whether nonlinear ultrasonic behavior evolves differently across distinct porosity interaction states. The identified clusters were interpreted as representing transitions from isolated pore behavior to interaction-dominated and spatially clustered defect-network regimes.

2.3 Acoustic Measurement and SPC-I Computation

The experimental configuration used for nonlinear ultrasonic testing, a broadband chirp excitation signal ranging from 0 to 350 kHz, which was generated using a BK Precision 4055B function generator and amplified to a peak-to-peak voltage of 20 V using a PD200 power amplifier. Two transducers were symmetrically attached to the opposite sides of the gauge section along the specimen diameter, as illustrated in the highlighted area in Figure 2. The amplified signal was transmitted through an Olympus piezoelectric (PZT) transducer, which converted the electrical excitation into an ultrasonic wave that propagated through the specimen. To ensure interaction between the ultrasonic wave and microstructural nonlinearities over a broad frequency range, the broadband chirp excitation was selected to stimulate multiple defect-sensitive frequency components and promote sideband generation. The transmitted wave was received by a second PZT transducer positioned on the opposite side of the specimen, and the resulting response signal was recorded using a Tektronix MDO3024 oscilloscope interfaced with a computer for data acquisition and processing. To facilitate direct comparison between the nonlinear ultrasonic measurements and the XCT-derived porosity characterization within the same region of interest, both transducers were mounted using a custom fixture that positioned them across the specimen gauge section. This configuration ensured stable acoustic coupling and consistent wave propagation through the central gauge region, where XCT-based porosity analysis was performed.

The hybrid ultrasonic responses were quantified using the Sideband Peak Count Index (SPC-I) as shown in Table 3, a nonlinear acoustic metric designed to capture cumulative nonlinear spectral activity. SPC-I is defined as:

$$\text{SPC-I} = \frac{1}{M}\left\{\sum_{i=1}^{M} N_{\text{peaks}}[A(f)] > T_i\right\} \qquad (2)$$

where $A(f)$is the amplitude spectrum of the measured signal, T_i is the predefined i-th threshold, and $N_{\text{peaks}}[A(f)] > T_i$ represents the number of spectral peaks exceeding the i-th threshold. M represents the total number of pre-defined threshold values. The computation involves signal acquisition in the time domain, transformation to the frequency domain using a Fast Fourier Transform (FFT), and threshold-based peak counting. To ensure the SPC-I is not affected by the intensity of signals varying between samples, the amplitude was normalized. The threshold line was moved between a preset upper and lower bounds in the normalized spectral plots. The upper bound was set at 1, and the lower bound was set at 0.065 to minimize counting the peaks from the

test noises. Previous studies have demonstrated that SPC-I is sensitive to crack initiation and growth, distributed defect interaction, stress-state variation, welded-joint degradation, and microstructural evolution [14,17–23]. In the present study, SPC-I is interpreted as a global hybrid ultrasonic response indicator reflecting cumulative defect interaction activity within the material rather than a direct measurement of individual microstructural features. Accordingly, the conceptual relationship between the hybrid ultrasonic response and the evolving material state is expressed as

$$M = f(\text{SPC-I}) \quad (3)$$

where (M) represents the evolving microstructural condition. Within this framework, SPC-I is treated as a first-stage screening metric for the defect activity, while XCT-derived descriptors and the physics-informed Porosity Index (PI) are used to improve interpretation of the underlying porosity state and defect interaction mechanisms.

2.4 Physics-Informed Porosity Index (PI)

The physics-informed Porosity Index (PI) is a composite descriptor that integrates hybrid ultrasonic measurements with normalized XCT-derived structure descriptors to facilitate structure-sensitive interpretation of porosity evolution. The PI framework was developed to capture the combined influence of pore size, porosity fraction, defect structure, spatial variability, and inter-defect interaction within a unified structure-sensitive descriptor.

In generalized form, the PI is expressed as:

$$PI = X_{i,\text{norm}} \times \text{SPC-I}_{\text{norm}} \quad (4)$$

$$\text{SPC-I}_{\text{norm}} = \frac{SPC\text{-}I_i}{SPC\text{-}I_{i,\text{ref}}} \quad (5)$$

where $X_{i,\text{norm}}$ represents a normalized porosity descriptor, $\text{SPC-I}_{\text{norm}}$ is the normalized hybrid ultrasonic response, and i is the sample number.

The selected descriptors were chosen to represent both morphological and spatial characteristics of the pore population. Based on feature sensitivity analysis and cluster-wise regression behavior, porosity volume fraction, maximum pore size, average pore size, pore size variability, and median inter-pore distance were identified as dominant contributors to the nonlinear response. Sphericity-related descriptors exhibited comparatively weaker influence and were therefore treated as secondary parameters.

The PI framework was further extended by constructing combined structure-sensitive descriptors using a multiplicative composite formulation. In this approach, all normalized porosity descriptors were multiplied together with the normalized SPC-I response to capture cumulative defect

interaction effects on nonlinear ultrasonic behavior. This dot-product formulation was motivated by the observation that porosity fraction alone is insufficient to explain the hybrid response in heterogeneous AM materials. Specimens exhibiting similar porosity fractions may display substantially different SPC-I behavior depending on pore structure, spatial clustering, and defect interaction state. The multiplicative structure of the PI therefore reflects the coupled contribution of structure-sensitive descriptors to the cumulative hybrid ultrasonic response. By integrating XCT-derived structure descriptors with SPC-I measurements, the proposed PI framework provides a mechanism-sensitive interpretation of evolving defect states in additively manufactured materials [6,14,15,17,20,26].

It should be noted that SPC-I is incorporated directly into the PI formulation as a structure-weighted hybrid response term. Consequently, PI is not intended to function as a statistically independent predictor of SPC-I. Rather, the index serves as a physics-informed interpretive framework that combines hybrid ultrasonic response with XCT-derived descriptors to represent the coupled effects of pore size evolution, structure irregularity, porosity variability, and spatial defect interaction. Therefore, correlations between SPC-I and PI should be interpreted primarily as indicators of the consistency between nonlinear ultrasonic behavior and structure-sensitive porosity evolution rather than as independent predictive relationships.

Finally, cluster-wise regression analysis was performed between SPC-I and the PI descriptors within each structure-derived cluster. This analysis was conducted to evaluate whether the relationship between hybrid ultrasonic response and porosity characteristics changes across different defect interaction regimes. Improved regression behavior within individual clusters compared with global regression was interpreted as evidence that SPC-I sensitivity is governed by evolving defect interaction mechanisms rather than a single uniform porosity-response relationship.

Table 2. Summary of material characteristics extracted from XCT analysis, including porosity volume fraction, pore size statistics (average, maximum, and standard deviation (SD)), and sphericity used to evaluate defect structure within the specimens.

Sample name	Max size of porosity	Avg size of porosity	Volume fraction	SD of the porosity size	Sphericity	SD of Sphericity	Median distance to the neighbor	SD of the distance to the neighbor	Epsilon	Distance at epsilon
1B	111.100	21.500	0.010	12.900	0.773	0.080	157.869	151.312	0.9940	830.40
7B	97.700	18.700	0.008	10.600	0.769	0.078	145.508	151.048	0.9660	577.38
19A	113.600	28.100	0.009	17.592	0.755	0.083	354.210	192.788	0.9800	796.61
8A	79.300	18.000	0.004	10.600	0.759	0.076	169.034	212.380	0.9780	876.88
9A	122.700	21.200	0.007	14.100	0.782	0.068	226.070	190.143	0.9860	850.70
14A	112.900	22.300	0.007	14.800	0.760	0.075	254.468	190.926	0.9900	861.72
16B	147.000	28.000	0.024	19.700	0.758	0.084	226.260	152.185	0.9870	696.14
63A	80.600	26.500	0.001	12.567	0.758	0.075	405.535	185.392	0.9400	1051.13
68B	84.800	26.000	0.003	14.400	0.783	0.076	366.594	180.879	0.9230	882.04
69B	189.000	44.600	0.020	22.097	0.743	0.081	313.832	180.476	0.9800	937.31
76B	77.900	26.000	0.002	11.408	0.783	0.070	335.822	201.300	0.9410	860.71
36B	101.000	30.800	0.007	13.337	0.779	0.070	200.590	175.018	0.9990	1208.99
49A	66.200	26.100	0.002	11.562	0.769	0.085	205.580	193.112	0.9330	785.85
70B	91.100	29.200	0.010	13.010	0.767	0.076	187.128	174.372	0.9710	590.94
KG146A	76.100	29.300	0.002	13.385	0.798	0.063	397.376	202.827	0.9850	1210.45
KG155B	69.100	23.600	0.001	9.644	0.776	0.074	254.920	194.565	0.9260	774.11
KG169B	166.400	38.700	0.021	18.737	0.759	0.080	212.402	156.003	0.9630	578.45
KG167B	112.600	36.000	0.010	15.690	0.787	0.072	221.026	171.120	0.9770	732.70
39B	89.600	31.700	0.003	13.828	0.784	0.086	346.538	187.659	0.9460	925.27
KG1 30B	80.639	27.439	0.006	12.169	0.772	0.071	174.876	155.683	0.9750	603.80
KG1 20A	90.905	26.852	0.006	11.577	0.773	0.074	176.531	170.777	0.9470	490.23
KG1 13B	148.907	49.774	0.082	23.417	0.762	0.076	161.250	111.711	0.9810	548.05
KG1 12A	136.100	42.200	0.064	22.290	0.770	0.070	163.613	119.327	0.9900	661.44
KG156B	85.500	29.300	0.005	12.962	0.781	0.072	201.247	150.917	0.9860	871.46
12A	120.020	47.225	0.037	20.532	0.783	0.066	183.056	142.080	0.9580	529.67
77A	111.242	32.252	0.023	15.354	0.759	0.077	151.652	118.780	0.9895	627.87
56A	90.157	31.110	0.009	12.263	0.770	0.075	192.820	163.317	0.9952	835.30
26A	83.558	29.278	0.004	12.317	0.775	0.083	280.059	194.574	0.9550	667.11
24B	84.692	29.567	0.003	12.881	0.784	0.069	340.858	258.779	0.9360	783.01

Table 3. Quantitative SPC-I results, including average peak counts and corresponding SPC index values for each specimen.

Sample name	SPC-I
1B	0.136
7B	0.114
19A	0.12
8A	0.1
9A	0.106
14A	0.12
16B	0.114
63A	0.087
68B	0.09
69B	0.142
76B	0.09
36B	0.101
49A	0.086
70B	0.1096
KG146A	0.084
KG155B	0.08
KG169B	0.127
KG167B	0.107
39B	0.103
KG1 30B	0.103
KG1 20A	0.145
KG1 13B	0.102
KG1 12A	0.13
KG156B	0.097
12A	0.12
77A	0.120
56A	0.094
26A	0.088
24B	0.083

2.5. Model and architecture for non-PI analysis

A machine-learning-assisted procedure was implemented to further examine the direct relationship between XCT-derived porosity descriptors and the acoustic response. The measured SPC-I was used as the response variable, while the input features consisted of porosity structure and spatial-distribution descriptors extracted from XCT data. These descriptors included the pore-size statistics, pore volume fraction, sphericity-related metrics, and nearest-neighbor distance-based descriptors. Because the experimental dataset contained a limited number of specimens, the machine-learning workflow was designed as an exploratory validation approach to assess whether the structure-sensitive feature space contained internally consistent relationships with SPC-I, rather than as a fully generalized predictive framework.

To reduce the sensitivity of the neural-network analysis to the limited number of experimental specimens, a Random Forest regression model was first trained using the original experimental dataset. The model learned the relationship between the XCT-derived porosity descriptors and the

measured SPC-I values, and was then used to generate additional interpolated samples within the range of the experimentally observed data. Model hyperparameters, including the number of trees, maximum tree depth, minimum number of samples required for node splitting, and minimum number of samples per terminal leaf, were selected using five-fold cross-validation based on the validation mean squared error. The model with the lowest validation error was retained for subsequent interpolation.

After training, the Random Forest model was used to generate interpolated synthetic feature vectors within the learned feature space. For each decision tree, training samples assigned to the same terminal leaf were grouped together, and the mean feature vector of each group was calculated to represent a local feature-space center. Small random perturbations were then added to these local centers to produce interpolated feature vectors. The trained Random Forest model was subsequently used to assign SPC-I values to the interpolated feature vectors, producing 1500 data for the following neural-network analyses. This interpolation procedure was intended to improve training stability and explore local trends within the experimentally sampled feature space; it was not used to claim extrapolative prediction beyond the measured porosity conditions.

The augmented dataset was then used for DNN-based regression and feature-importance analysis. Prior to training, both the input features and SPC-I values were standardized. The DNN was trained to predict continuous SPC-I values using mean squared error as the loss function and the Adam optimizer. Early stopping based on the validation loss was applied to reduce overfitting. Feature importance was evaluated using a permutation-based approach. In this procedure, each input feature was independently shuffled while the remaining features were kept unchanged, and the corresponding increase in prediction error was used to estimate the relative contribution of that feature to the learned SPC-I response. The DNN architecture and prediction results are presented in the following section.

3. Results

3.1 Regression-Based Relationship Between SPC-I and XCT-Derived Porosity Descriptors

To investigate the sensitivity of hybrid ultrasonic response to porosity characteristics, linear regression analysis was performed between the normalized Sideband Peak Count Index (SPC-I) and all normalized XCT-derived descriptors, including both individual porosity parameters and physics-informed Porosity Index (PI) formulations. The implemented regression workflow automatically evaluated each descriptor against SPC-I and generated scatter plots with regression fits and coefficient-of-determination (R^2) values.

The regression model was expressed as:

$$Yi = a(SPC - I) + b \quad (6)$$

where Yi represents either an individual XCT-derived descriptor or a physics-informed porosity index, and a and b are regression coefficients.

The regression results demonstrated that SPC-I exhibits measurable correlation with several structure-sensitive porosity descriptors. Stronger relationships were observed for descriptors associated with pore size evolution and pore size variability, including maximum pore size (S_{max}), average pore size (S_{avg}), and pore size standard deviation (σ_{size}). By contrast, descriptors associated primarily with pore spacing or isolated spatial metrics exhibited comparatively weaker global correlations. As expected from the multiplicative PI definition, several SPC-I-weighted descriptors exhibited high correlations with SPC-I. These correlations do not establish independent predictive relationships and should not be used alone to rank the physical influence of XCT descriptors. Rather, they quantify how strongly each XCT descriptor modulates the SPC-I-weighted composite response. This outcome suggests that hybrid ultrasonic response is governed by coupled interactions among pore size evolution, defect density, structure irregularity, and distributed defect interaction rather than by any single porosity descriptor independently.

From a physical standpoint, these observations are consistent with nonlinear ultrasonic theory and previously reported SPC-I behavior [13–21,23]. Larger and more irregular pores generate stronger local stress concentrations and intensify nonlinear wave modulation, harmonic distortion, and spectral sideband generation. Increased pore-size variability further enhances distributed scattering and localized nonlinear interaction effects, thereby increasing SPC-I sensitivity. As shown in Table 4 and Figures 4 and 5, incorporation of SPC-I into the PI formulation increased the observed correlations; therefore, these results should be interpreted as measures of consistency between acoustic response and porosity descriptors rather than independent predictive relationships. Increases in the coefficient of determination were observed after SPC-I was incorporated into the composite descriptors; however, these increases partly reflect the mathematical coupling introduced by the PI definition. In particular, the correlation associated with maximum pore size increased from 0.46 to 0.70, average pore size increased from 0.07 to 0.44, and pore-size standard deviation increased from 0.24 to 0.59. Similarly, strong improvements were observed for structure-related descriptors, with sphericity increasing from 0.22 to 0.99 and the standard deviation of sphericity increasing from 0.044 to 0.86. The epsilon-related descriptor also exhibited a substantial increase from 0.18 to 0.98.

More moderate improvements were observed for porosity volume fraction and the standard deviation of nearest-neighbor distance, with ($\mathbf{R^2}$) values increasing from 0.12 to 0.18 and from 0.23 to 0.25, respectively. In contrast, descriptors associated primarily with pore-spacing metrics showed limited improvement or a slight reduction in correlation. Specifically, the median nearest-neighbor distance decreased from 0.17 to 0.017, while the distance-at-epsilon parameter decreased slightly from 0.15 to 0.11.

These results indicate that SPC-I is more strongly influenced by pore structure evolution, pore-size variability, and cumulative defect interaction mechanisms than by spatial spacing metrics alone. The improved correlations obtained using PI descriptors further support the interpretation that nonlinear acoustic behavior arises from coupled and cumulative defect interactions rather than isolated porosity features individually. It should also be noted that SPC-I is mathematically

incorporated within the PI formulation itself. Consequently, the exceptionally high correlations observed for several PI descriptors partially reflect the coupled mathematical structure of the constructed index in addition to the underlying physical relationship between hybrid ultrasonic response and porosity evolution. Therefore, the PI framework should be interpreted primarily as a physics-informed structure-sensitive representation that improves interpretability and clustering consistency rather than as a purely independent predictive variable. Regression plots are shown in Figures 4 and 5.

Because each PI descriptor is defined as the product of normalized SPC-I and an XCT-derived parameter, the PI–SPC-I coefficient of determination depends partly on the variability of the corresponding XCT descriptor. If an XCT parameter remains nearly constant across specimens, the associated PI becomes approximately proportional to SPC-I and may consequently produce an R^2 value approaching unity. Therefore, the high R^2 values obtained for PI-sphericity and PI-epsilon should not be interpreted as evidence that these descriptors are the strongest physical determinants of SPC-I. Instead, descriptor influence should be evaluated using the direct XCT-SPC-I regressions, descriptor variability, cluster-average trends, and the independent XCT-only versus SPC-I-weighted clustering comparison. Within this study, the PI is used as a data-fusion and regime-interpretation parameter rather than an independent predictive model.

Table 4. Linear regression results for XCT-derived porosity descriptors and physics-informed porosity index (PI) descriptors relative to normalized SPC-I(SPC-I/SPC-I(49A))

XCT-derived porosity descriptors	**Y Column**	**X Column**	**Slope**	**Intercept**	**R^2**
	Max size of porosity	*normalized SPC-I*	1.45	-0.23	0.46
	Avg size of porosity	*normalized SPC-I*	0.40	0.66	0.08
	Volume fraction (VF)	*normalized SPC-I*	13.51	-10.97	0.12
	SD of the porosity size	*normalized SPC-I*	0.76	0.32	0.24
	Sphericity	*normalized SPC-I*	-0.03	1.05	0.22
	SD of Sphericity	*normalized SPC-I*	0.07	0.80	0.04
	Median distance to the neighbor	*normalized SPC-I*	-0.78	2.14	0.18
	SD of the distance to the neighbor	*normalized SPC-I*	-0.37	1.35	0.24
	epsilon	*normalized SPC-I*	0.05	0.98	0.18
	distance at epsilon	*normalized SPC-I*	-0.44	1.54	0.16
Porosity Index (PI) descriptors	PI, all	*normalized SPC-I*	90.92	-95.10	0.23
	PI, VF	*normalized SPC-I*	22.00	-19.53	0.18
	PI, std of the distance to neighbor	*normalized SPC-I*	0.47	0.52	0.26
	PI, median distance of the porosity to the neighbor	*normalized SPC-I*	0.27	1.09	0.02
	PI, Standard deviation of sphericity	*normalized SPC-I*	0.97	-0.11	0.86
	PI, sphericity	*normalized SPC-I*	0.96	0.06	0.99
	PI, Standard deviation of the porosity size	*normalized SPC-I*	2.22	-1.15	0.59
	PI, avg size of porosity	*normalized SPC-I*	1.67	-0.63	0.44
	PI, max size of porosity	*normalized SPC-I*	3.45	-2.26	0.70
	PI, Distance at epsilon	*normalized SPC-I*	0.44	0.66	0.11
	PI, epsilon	*normalized SPC-I*	1.09	-0.07	0.99

Coefficient of variation (CV) analysis was performed for all XCT-derived descriptors to distinguish physically meaningful SPC-I–porosity relationships from correlations introduced by the PI formulation (Table 5). The results show that descriptors such as sphericity (CV = 1.57%) and epsilon (CV = 2.36%) exhibit very limited specimen-to-specimen variability. Because each PI descriptor is defined as the product of the normalized SPC-I and the corresponding normalized XCT descriptor, descriptors with low variability behave approximately as constant multipliers of SPC-I, naturally producing PI–SPC-I coefficients of determination approaching unity. Consequently, the exceptionally high R^2 values obtained for PI–sphericity and PI–epsilon should not be interpreted as evidence that these descriptors independently govern the hybrid ultrasonic response. Instead, the direct XCT–SPC-I regressions provide the appropriate measure of the independent association between each XCT descriptor and SPC-I, whereas the PI descriptors are intended to integrate multiple sources of information for structure-sensitive interpretation rather than to establish independent predictive relationships.

Table 5. XCT Descriptor Variability and SPC-I Correlation Summary

XCT descriptor	Mean	Standard deviation	CV (%)	Direct XCT–SPC-I R^2	PI–SPC-I R^2
Maximum pore size	1.5733	0.4520	28.73	0.4639	0.7031
Average pore size	1.1511	0.3054	26.53	0.0761	0.4405
Porosity volume fraction	5.8120	8.1058	139.47	0.1245	0.1830
Standard deviation of pore size	1.2697	0.3281	25.84	0.2426	0.5914
Sphericity	1.0034	0.0157	**1.57**	0.2205	**0.9923**
Standard deviation of sphericity	0.8834	0.0694	**7.86**	0.0440	**0.8621**
Median nearest-neighbor distance	1.1753	0.3924	33.39	0.1766	0.0171
Standard deviation of nearest-neighbor distance	0.8981	0.1594	17.75	0.2377	0.2565
Epsilon	1.0377	0.0245	**2.36**	0.1840	**0.9876**
Distance at epsilon	0.9937	0.2343	23.58	0.1568	0.1096

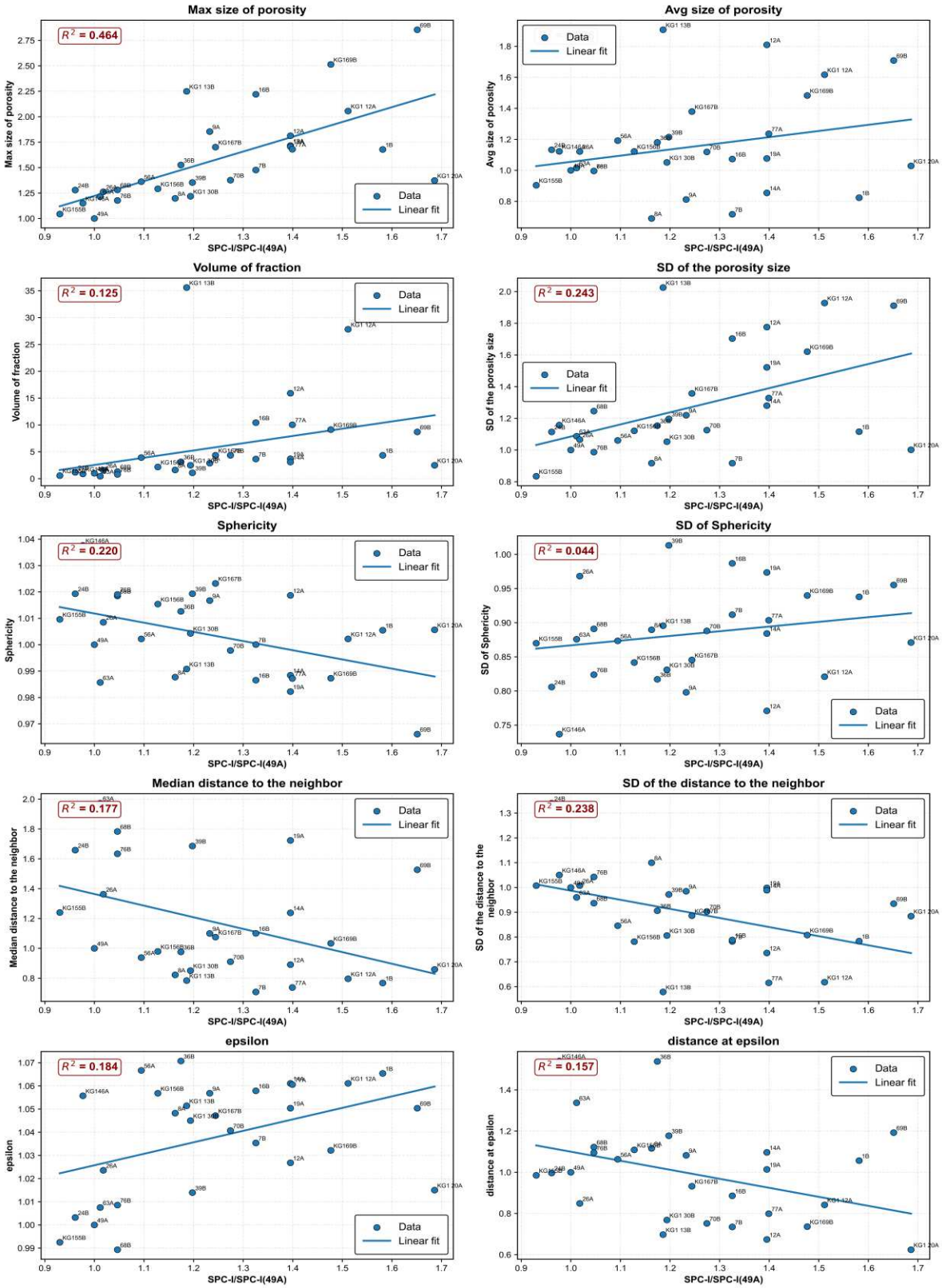

Figure 4. Linear regression plots between normalized XCT-derived porosity descriptors and normalized SPC-I

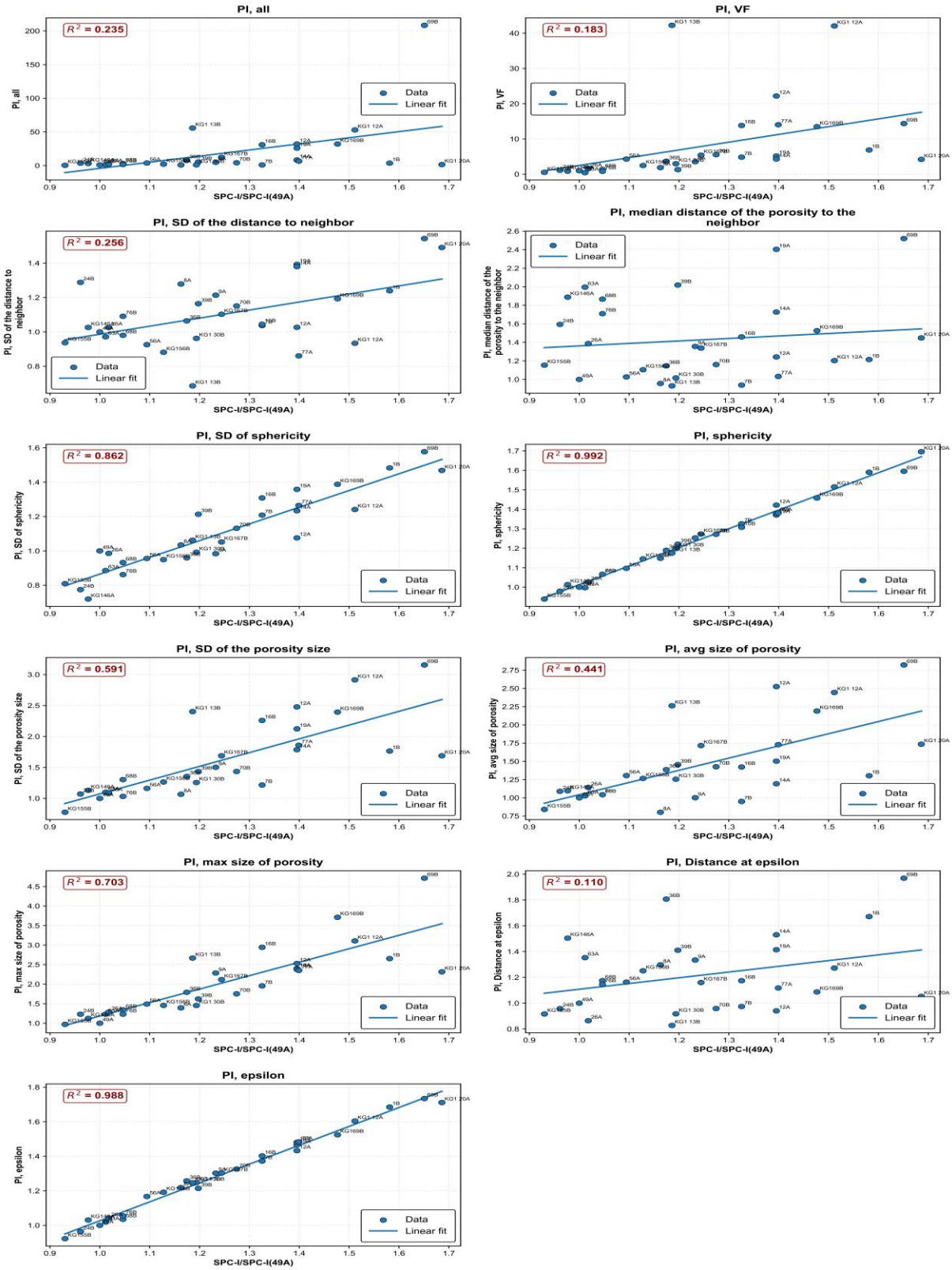

Figure 5. Linear regression relationships between physics-informed porosity index (PI) descriptors and normalized SPC-I

3.2 Principal Component Analysis of Porosity Structures

Because the XCT-derived dataset contains multiple correlated porosity descriptors, Principal Component Analysis (PCA) was employed to reduce the dimensionality of the structure feature space while preserving the dominant variance among specimens. Prior to PCA, all XCT-derived descriptors were standardized to zero mean and unit variance using z-score normalization to eliminate scale dependency and ensure equal contribution of each feature to the covariance structure. The resulting principal components provide an orthogonal representation of the multidimensional porosity dataset and facilitate visualization of structure-dependent trends. The first two principal components accounted for 69.6% of the total dataset variance, with PC1 explaining 50.1% and PC2 explaining 19.6%, as summarized in Table 6. PC1 was primarily associated with pore-size evolution, porosity volume fraction, and pore-size variability, whereas PC2 mainly represented secondary variations related to pore structure and spatial organization. These results indicate that the dominant variability among specimens is controlled primarily by defect size and structure rather than by isolated spatial descriptors alone.

The PCA projection shown in Figure 6 provides the first visualization of the specimen distribution within the reduced structure feature space. Three groups of specimens naturally emerge in the PC1–PC2 domain, indicating that the XCT-derived descriptors contain sufficient information to distinguish different porosity regimes before any interpretation of the hybrid ultrasonic response. These preliminary groupings served as the basis for the subsequent clustering analysis.

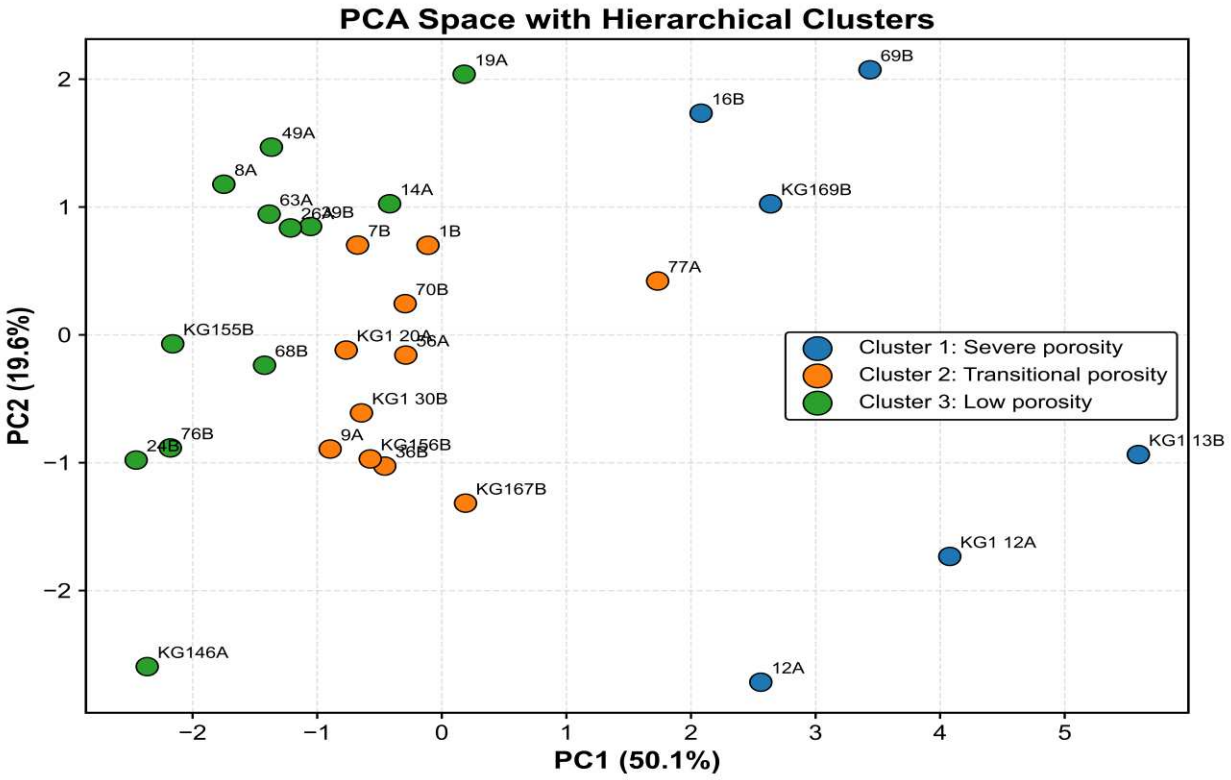

Figure 6. Principal Component Analysis (PCA) projection of normalized XCT-derived porosity descriptors with hierarchical cluster assignments

Table 6. Principal Component Analysis (PCA) explained variance ratios and cumulative variance contribution of normalized XCT-derived porosity descriptors.

PC	Explained Variance Ratio	Cumulative Explained Variance
PC1	0.501	0.501
PC2	0.195	0.697
PC3	0.158	0.855
PC4	0.056	0.911
PC5	0.0334	0.944
PC6	0.029	0.974
PC7	0.022	0.995
PC8	0.0045	1

To further define the separation between these structure regimes, K-means classification was applied in the reduced PCA space to construct the decision boundaries shown in Figure 7. Each colored region represents the set of specimens assigned to the nearest cluster centroid based on Euclidean distance in the principal-component space. Although some specimens appear close to each other in the two-dimensional projection, their final assignments may differ because clustering was originally performed using the complete standardized XCT feature matrix rather than only the first two principal components. Consequently, Figure 7 provides an interpretable two-dimensional visualization of the multidimensional structure space while preserving the original clustering results. To verify that the PCA-based groupings represented intrinsic similarities in the XCT descriptors, hierarchical clustering using Ward linkage was subsequently performed. The resulting dendrogram (Figure 8) shows that specimens with similar pore structure are progressively merged into common branches while minimizing within-cluster variance. The dendrogram independently confirms the presence of three dominant structure-dependent clusters, supporting the PCA-based classification and indicating that the observed grouping is robust rather than an artifact of dimensionality reduction.

The average normalized descriptor values for each hierarchical cluster are summarized in Table 7, which provides the physical basis for interpreting the three structure regimes. Cluster 1 exhibits the largest normalized pore size, porosity fraction, pore-size variability, and structure-related descriptors, indicating severe porosity characterized by large, irregular, and interacting defect networks. Cluster 2 represents an intermediate or transitional structure state with moderate pore growth and increasing defect interactions. Cluster 3 is characterized by comparatively smaller pore sizes, lower porosity levels, and more uniformly distributed pores, corresponding to an isolated-defect regime. These quantitative differences demonstrate that the identified clusters are physically meaningful and represent successive stages of porosity evolution rather than arbitrary statistical groupings.

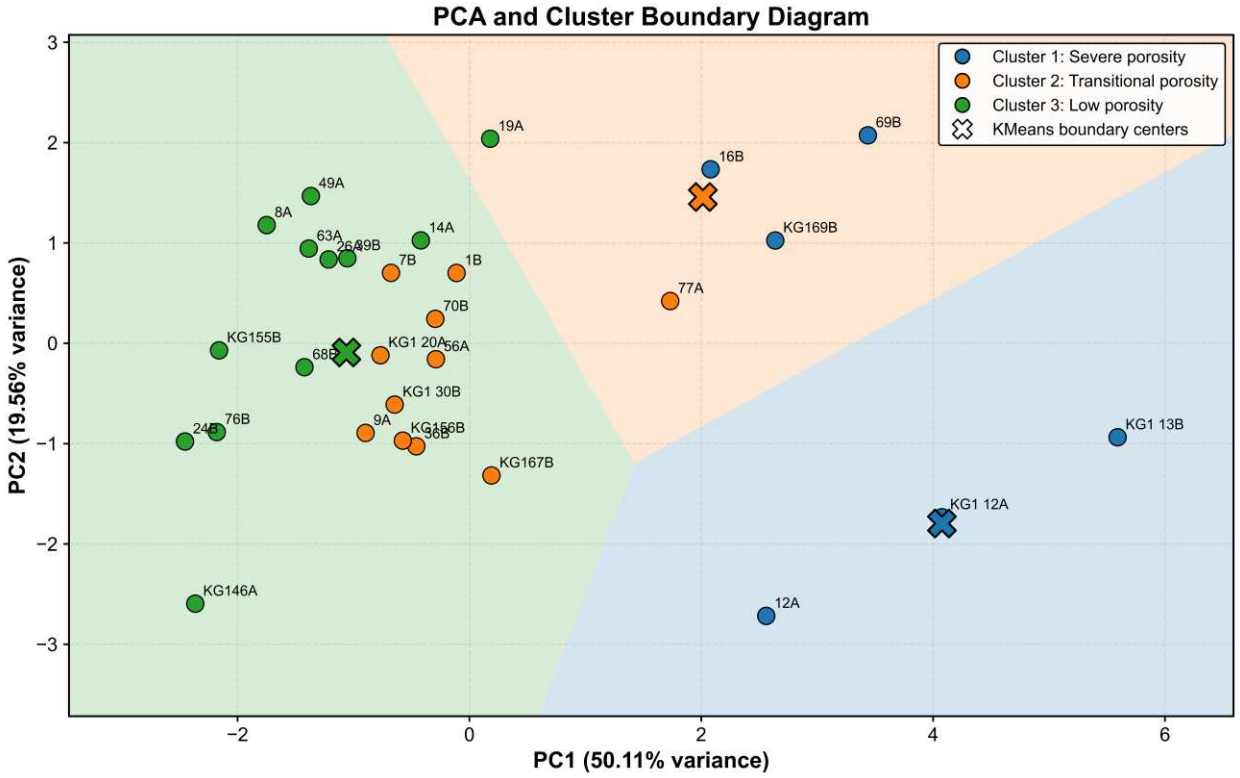

Figure 7. PCA-based cluster boundary diagram showing structure-dependent separation of porosity regimes

To validate PCA results, unsupervised clustering analysis was performed using hierarchical clustering with Ward linkage to identify natural groupings within the normalized porosity descriptor space. Clustering was conducted exclusively using the standardized XCT-derived feature matrix without inclusion of SPC-I, allowing the hybrid ultrasonic response to be evaluated independently relative to the identified structure regimes. The resulting clustering structures are summarized in Tables 6–8 and visualized in Figures 6–8. To evaluate clustering quality and determine the optimal number of clusters, the silhouette coefficient was employed, as shown in Table 8:

$$s = \frac{b-a}{\max(a,b)} \quad (7)$$

where a represents the mean intra-cluster distance and b represents the nearest-cluster distance. Although the silhouette values are moderate, they are consistent with partially overlapping microstructural populations commonly observed in AM porosity datasets. Collectively, the PCA projection, boundary classification, hierarchical dendrogram, and cluster statistics demonstrate that the XCT-derived descriptors effectively capture the dominant physical mechanisms governing porosity evolution in additively manufactured IN718. The identified structure regimes provide the foundation for the subsequent analyses, where the hybrid ultrasonic SPC-I response is evaluated relative to physically distinct porosity states rather than across the heterogeneous dataset as a whole.

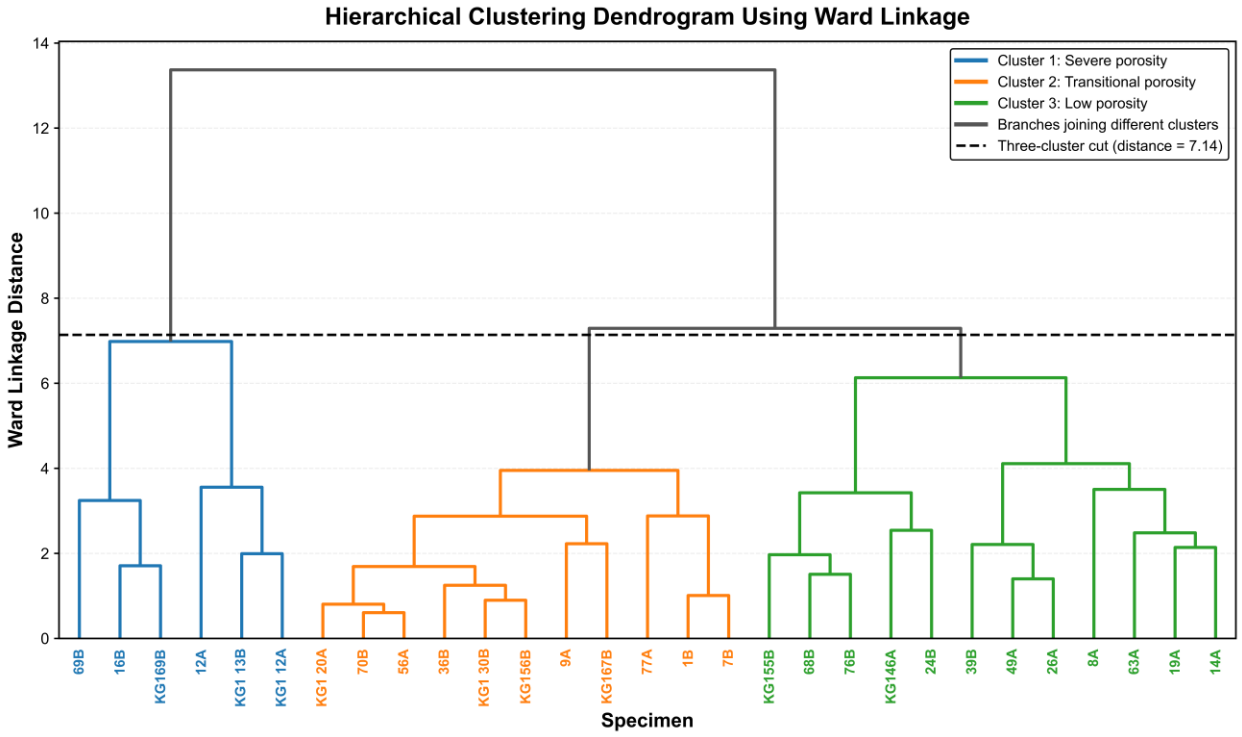

Figure 8. Hierarchical clustering dendrogram obtained using Ward linkage. A horizontal cut at the selected linkage distance yields three morphology-based clusters that correspond to the porosity regimes identified by the PCA and K-means analyses. The branch colors represent the three final clusters used throughout the subsequent regression and statistical analyses.

Table 7. Average normalized XCT-derived descriptor values for the three hierarchical clusters.

Hierarchical Cluster	Max size of porosity	Avg size of porosity	Volume fraction	SD of the porosity size	Sphericity	SD of Sphericity	Median distance to the neighbor	SD of the distance to the neighbor	epsilon	distance at epsilon
1	2.285	1.600	17.933	1.827	0.992	0.895	1.022	0.744	2.285	1.600
2	1.503	1.060	3.983	1.132	1.006	0.865	0.900	0.834	1.503	1.060
3	1.282	1.010	1.429	1.117	1.006	0.894	1.504	1.034	1.282	1.010

Table 8. Comparison of silhouette scores for K-means and hierarchical clustering methods

Method	Number of Clusters	Silhouette Score
KMeans	3	0.35
Hierarchical Ward	3	0.21

Through hierarchical clustering, three clusters can also be identified, providing the best balance between cluster compactness and inter-cluster separation. By looking into the samples in each

cluster, these clusters are found to correspond to certain types of porosity structures, as demonstrated in Table 9 [27–29].

Table 9. Pore structure characteristics observed from each cluster defined by PCA, hierarchical clustering, and Porosity structure

Cluster	**Structural Interpretation**
Cluster 1	Generally having larger numbers of porosity with large, irregular, and clustered defects
Cluster 2	Transitional porosity state with moderate pore growth and variability
Cluster 3	Generally having smaller numbers of porosity with small and uniformly distributed pores

3.3 Comparison of XCT-Only and SPC-I-Weighted Clustering

To evaluate whether inclusion of SPC-I provides additional discriminatory information beyond XCT-derived structure descriptors alone, clustering analyses were performed using (i) XCT-only descriptors and (ii) SPC-I-weighted PI descriptors. As shown in Figure 9, the SPC-I-weighted framework produced a higher silhouette score (0.3337 versus 0.3144), a stronger separation of cluster-average SPC-I values (ANOVA $p < 0.0001$ versus $p = 0.0023$), and a substantially larger average cluster-wise R^2 improvement (0.1135 versus 0.0461). These results indicate that incorporation of SPC-I enhances the identification of structure-dependent defect interaction regimes. The improvement suggests that SPC-I provides information on cumulative hybrid acoustic behavior that is not fully captured by XCT-derived geometric descriptors alone, thereby strengthening the physical basis of the proposed PI framework. This comparison evaluates the contribution of SPC-I to regime classification and should be distinguished from PI–SPC-I regression, whose magnitude is partly governed by the mathematical inclusion of SPC-I in the PI definition.

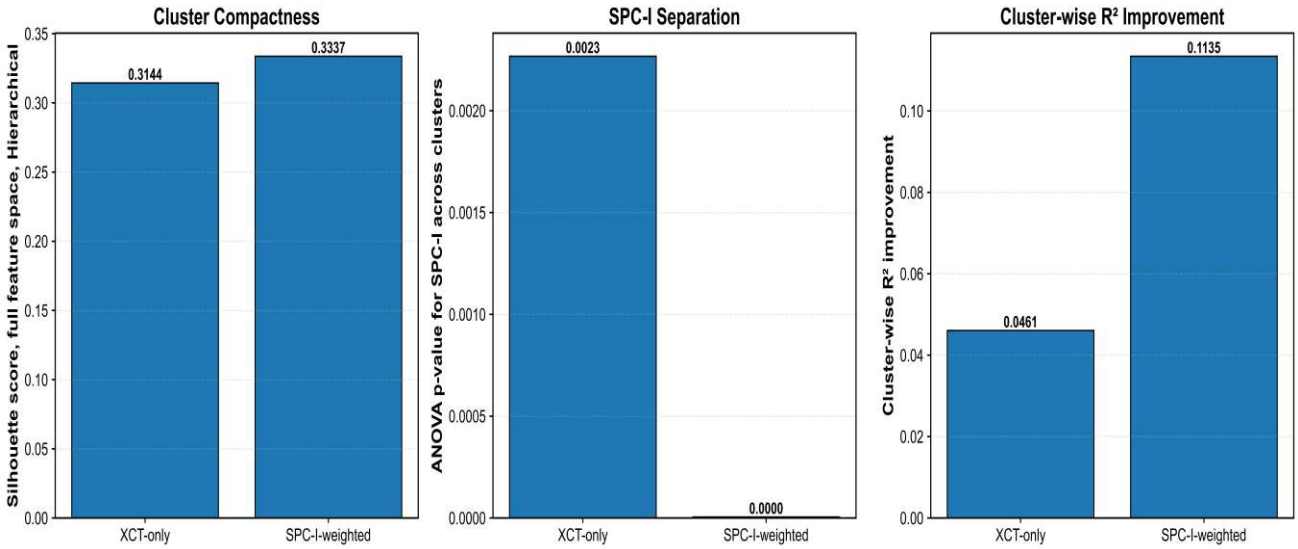

Figure 9. Comparison of XCT-only and SPC-I-weighted clustering frameworks

3.4 Cluster-Wise Regression Between SPC-I and PI Descriptors

To investigate whether the relationship between ultrasonic response and porosity structure depends on the underlying defect regime, cluster-wise linear regression analysis was performed between SPC-I and each physics-informed porosity index (PI) descriptor within the three structure-derived clusters (Figure 10). The resulting coefficients of determination (R^2) are summarized in Table 10 and compared with the corresponding global regression values obtained using the complete dataset. A descriptor was considered cluster-sensitive when its cluster-wise R^2 exceeded the corresponding global R^2 value. The results demonstrate that most descriptors exhibit stronger correlations within individual clusters than across the entire dataset, indicating that the SPC-I–porosity relationship is regime-dependent rather than globally uniform.

For Cluster 1, the strongest correlations were observed for PI based on sphericity ($R^2 = 0.974$), epsilon ($R^2 = 0.984$), standard deviation of distance to neighbors ($R^2 = 0.704$), standard deviation of sphericity ($R^2 = 0.628$), and median nearest-neighbor distance ($R^2 = 0.603$). These results suggest that the ultrasonic response in Cluster 1 is governed primarily by pore structure and spatial organization rather than porosity size and structure. The strong influence of sphericity-related descriptors indicates that local geometric irregularity plays a dominant role in sideband generation.

For Cluster 2, the highest correlations were obtained for epsilon ($R^2 = 0.988$), sphericity ($R^2 = 0.997$), standard deviation of sphericity ($R^2 = 0.945$), and standard deviation of nearest-neighbor distance ($R^2 = 0.763$). This cluster, therefore, represents a transitional regime in which evolving pore structure and increasing spatial interaction begin to influence the hybrid ultrasonic response. The simultaneous importance of structure and spacing descriptors suggests the initiation of defect interaction effects.

For Cluster 3, the strongest relationships were observed for maximum pore size ($R^2 = 0.938$), epsilon ($R^2 = 0.988$), sphericity ($R^2 = 0.989$), standard deviation of pore size ($R^2 = 0.834$), porosity volume fraction ($R^2 = 0.844$), and standard deviation of sphericity ($R^2 = 0.835$). Compared with the global regressions, these substantial increases indicate that Cluster 3 is characterized by strong individual pore contributions associated with large defects, increased volume fraction and pore-size variability, while weaker contributions from clustering behaviors ($R^2 < 0.844$). The dominant influence of pore-size descriptors suggests that nonlinear scattering and local stress-concentration effects become dominant in this regime.

Overall, the cluster-wise regressions reveal that different porosity descriptors govern SPC-I sensitivity within different pore structure regimes. While global regression masks these relationships due to the dataset's heterogeneity, cluster-wise analysis isolates physically similar defect populations and yields markedly stronger correlations. These findings support the interpretation that SPC-I is controlled by evolving defect interaction mechanisms and structure-dependent behavior rather than by the pore size or the volume fraction alone.

The exceptionally high R^2 values observed for several PI descriptors, particularly those involving epsilon and sphericity, should be interpreted with appropriate caution. Because SPC-I is mathematically embedded within the PI construction, part of the observed correlation reflects the inherent coupling between the ultrasonic measurement and the composite index. Nevertheless, the substantial improvement of cluster-wise regression relative to global regression suggests that the identified structure-dependent regimes contain physically meaningful information beyond the mathematical structure of the PI formulation. The clustering results therefore support the interpretation that evolving pore structure and defect interaction mechanisms influence SPC-I behavior in a regime-dependent manner.

Table 10. Comparison of global and cluster-wise R^2 values for SPC-I–PI regression analysis

Model	**Cluster-wise**			**Global**
Cluster	**1**	**2**	**3**	**All**
PI, Distance at epsilon	0.712011	0.001995	0.422022	0.10958
PI, Standard deviation of sphericity	0.628327	0.945066	0.834595	0.862055
PI, Standard deviation of the porosity size	0.416611	0.543049	0.833541	0.591388
PI, VF	0.129035	0.273168	0.843836	0.182998
PI, all	0.398388	0.057086	0.575674	0.2346
PI, avg size of porosity	0.285369	0.120608	0.385868	0.440544
PI, epsilon	0.983868	0.987901	0.98777	0.987584
PI, max size of porosity	0.581978	0.617858	0.937984	0.703146
PI, median distance of the porosity to the neighbor	0.602963	0.284122	0.192155	0.017056
PI, sphericity	0.97366	0.997356	0.989413	0.992315
PI, std of the distance to neighbor	0.703992	0.762959	0.634962	0.256455

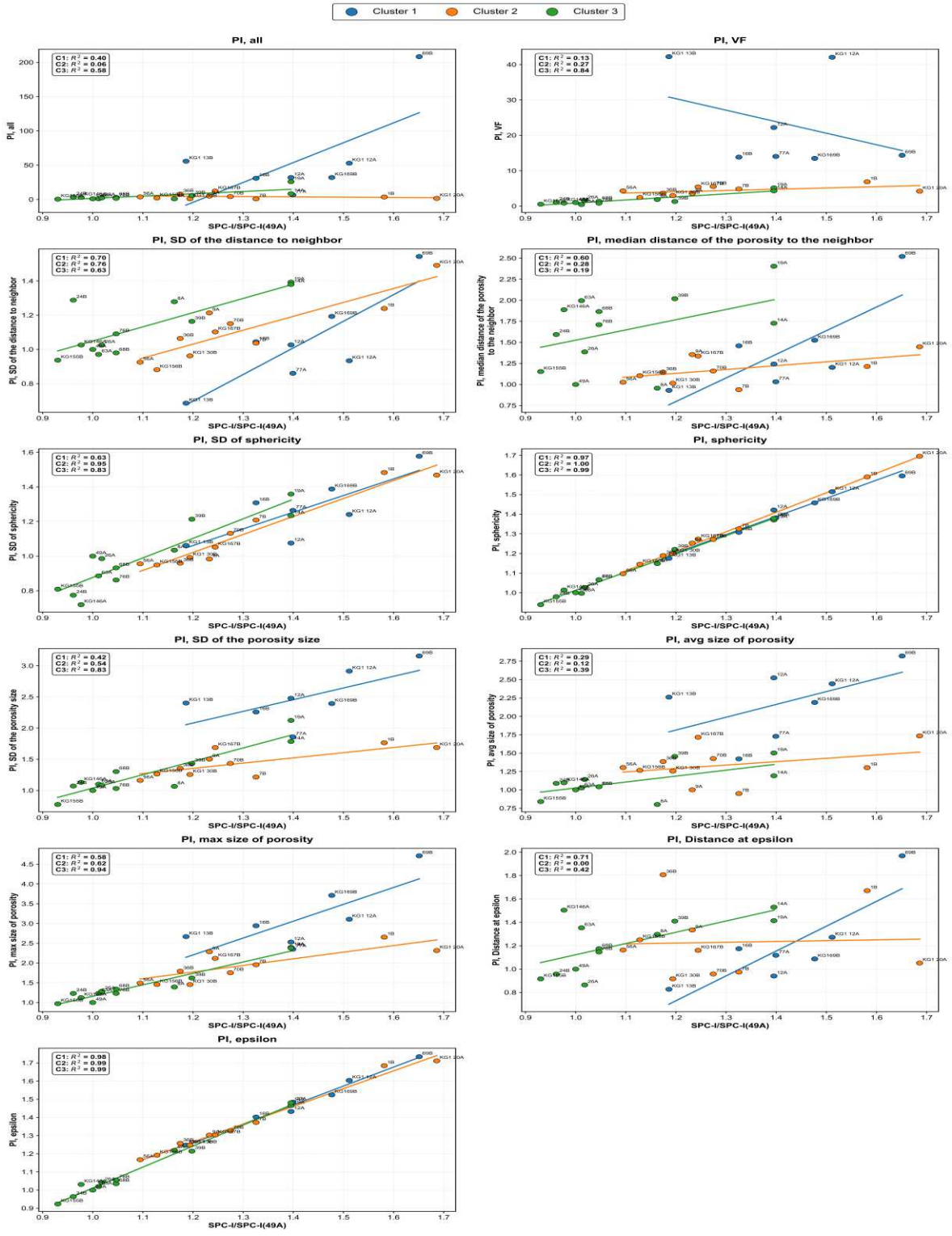

Figure 10. Combined cluster-wise regression plots between physics-informed porosity index (PI) descriptors and normalized SPC-I

3.4 Statistical Validation of Clustered SPC-I Behavior

To evaluate whether the structure-derived clusters correspond to statistically distinct acoustic states, the normalized SPC-I distributions were examined using boxplot visualization (Figure 11), one-way ANOVA, and Tukey post-hoc pairwise comparisons (Tables 10 and 11). The cluster-average SPC-I values exhibited a gradual decrease from approximately 1.42 in Cluster 1 to approximately 1.09 in Cluster 3. Although some variability and outliers were present, most specimens within each cluster exhibited SPC-I values concentrated around their corresponding cluster means, suggesting internally consistent acoustic behavior within each structure regime [29]

The one-way ANOVA was performed to assess the null hypothesis:

$$H_0: \mu_1 = \mu_2 = \mu_3 \quad (8)$$

Where $\mu_1, \mu_2, and\ \mu_3$ denote the mean SPC-I values of Clusters 1, 2, and 3, respectively. As shown in Table 11, the ANOVA yielded an F-statistic of 8.586 and a p-value of 0.0014, indicating statistically significant differences among cluster means at the 95% confidence level. Therefore, the null hypothesis was rejected, confirming that the clustering framework successfully separates specimens into distinct acoustic states.

To identify which cluster pairs contributed to the observed differences, Tukey post-hoc analysis was performed (Table 12). The results showed no statistically significant difference between Clusters 1 and 2 (p=0.3547), whereas significant differences were observed between Clusters 1 and 3 (p=0.0019) and between Clusters 2 and 3 (p=0.0189). These findings indicate that the low-porosity regime represented by Cluster 3 exhibits a statistically distinct SPC-I response from both Clusters 1 and 2, whereas the severe and transitional regimes represented by Clusters 1 and 2 exhibit partially overlapping SPC-I responses.

From a physical perspective, the statistical results suggest that Cluster 2 functions as a transitional porosity regime between isolated defect behavior (Cluster 3) and strongly interaction-dominated defect networks (Cluster 1). The significant separation of Cluster 1 from the other groups supports the interpretation that increasing pore growth, structure irregularity, and defect interaction collectively amplify acoustic effects and alter SPC-I behavior. These results provide quantitative evidence that the PI-based clustering framework captures physically meaningful porosity-interaction regimes and further support the use of SPC-I as a rapid screening indicator of evolving porosity state and defect interaction activity.

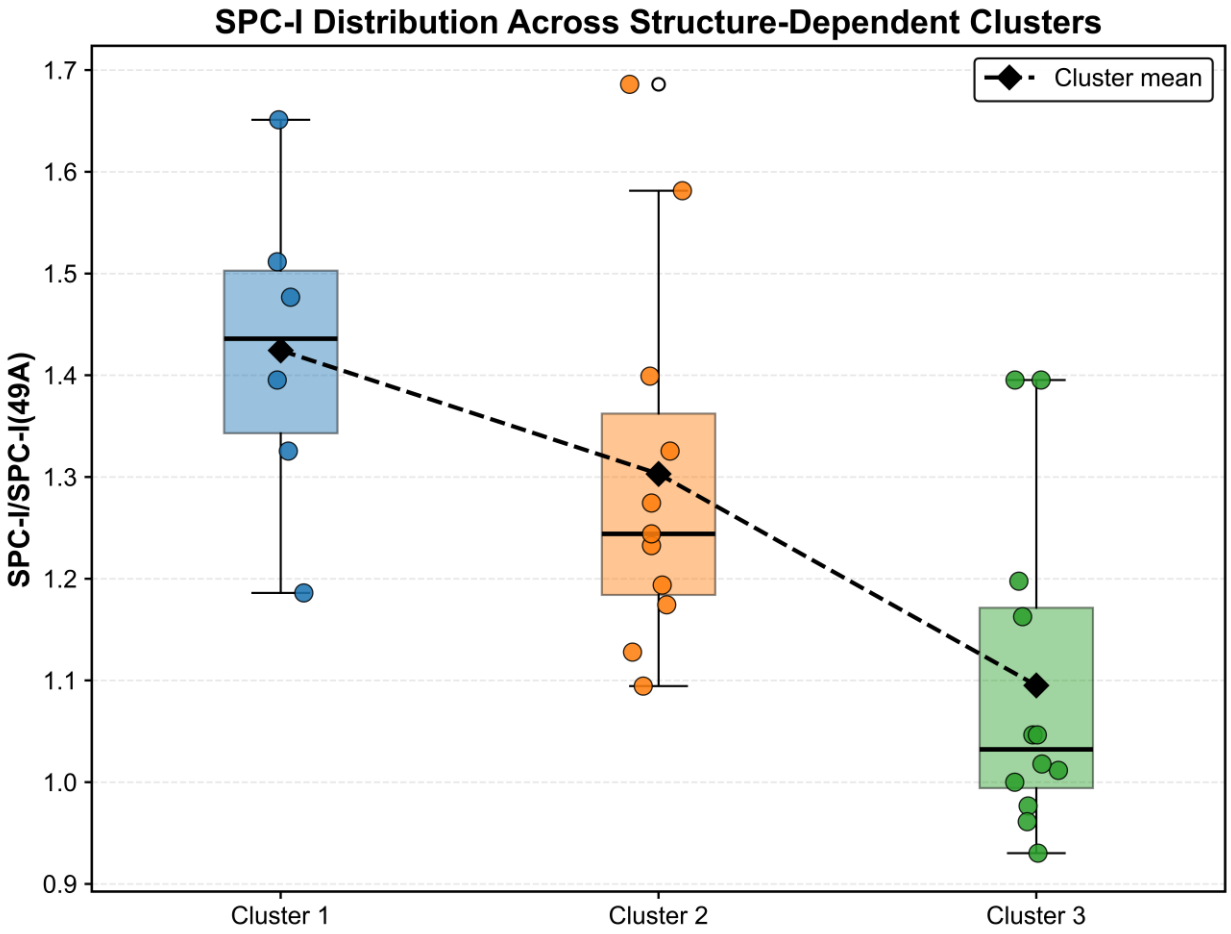

Figure 11. Distribution of normalized SPC-I across structure-dependent porosity clusters

Table 11. One-way ANOVA results for normalized SPC-I across structure-dependent clusters

Statistic	**p-value**
8.586	0.0014

Table 12. Tukey post-hoc pairwise comparison of normalized SPC-I among structure-dependent clusters

group1	**group2**	**meandiff**	**p-adj**	**lower**	**upper**	**reject**
1	2	-0.1213	0.3547	-0.3364	0.0938	FALSE
1	3	-0.3293	0.0019	-0.5411	-0.1174	TRUE
2	3	-0.2079	0.0189	-0.3848	-0.031	TRUE

3.6 Machine-Learning-Based Validation with the Full Dataset

The machine-learning analysis was conducted primarily as a complementary validation tool to support the experimentally observed relationships between hybrid ultrasonic response and XCT-derived porosity characteristics, as shown in Figure 12. Because the original experimental dataset consisted of only 29 specimens, the machine-learning results should be interpreted as exploratory and supportive of the underlying physical trends rather than as a fully validated predictive framework. To improve training stability and reduce sensitivity to the limited dataset size, a Random Forest-based interpolation approach was employed to augment the structure-sensitive feature space. Within this exploratory framework, whose architecture is illustrated in Figure 12 (a), the exploratory DNN achieved an approximately 80% prediction accuracy within the augmented feature space, which contains internally consistent relationships that can be learned within the available dataset, including maximum size, VF, SD of pore size, and distances to neighbors (see Figures 12 (b) and 12 (c)). However, given the small number of experimentally measured specimens and the use of augmented training data, this performance should not be interpreted as evidence of fully generalized predictive capability. Instead, the results indicate that internally consistent and learnable relationships exist between hybrid ultrasonic response and the XCT-derived porosity descriptors within the available feature space. This interpretation is consistent with previous studies employing machine-learning techniques to investigate structure–property relationships in additive manufacturing defect characterization [16,22,23].

Importantly, the machine-learning results were physically consistent with the experimentally derived SPC-I, PI, PCA, and clustering analyses. Feature-importance evaluation identified pore size distribution, maximum pore size, porosity volume fraction, pore size variability, and spatial clustering characteristics as the dominant contributors governing the hybrid ultrasonic response. These trends, shown in Figure 12, support the interpretation that SPC-I is governed primarily by structure-driven stress concentration, pore growth, and cumulative defect interaction mechanisms, with secondary contributions from pore shape and spatial organization.

The agreement between the machine-learning feature rankings and the experimentally motivated PI framework provides additional confidence that the proposed PI captures physically meaningful aspects of porosity-sensitive nonlinear ultrasonic behavior. Most importantly, the machine-learning analysis reinforces the broader interpretation that the hybrid ultrasonic response evolves systematically with defect structure and interaction state rather than with porosity quantity alone. Future validation using independent experimental datasets is required before predictive deployment.

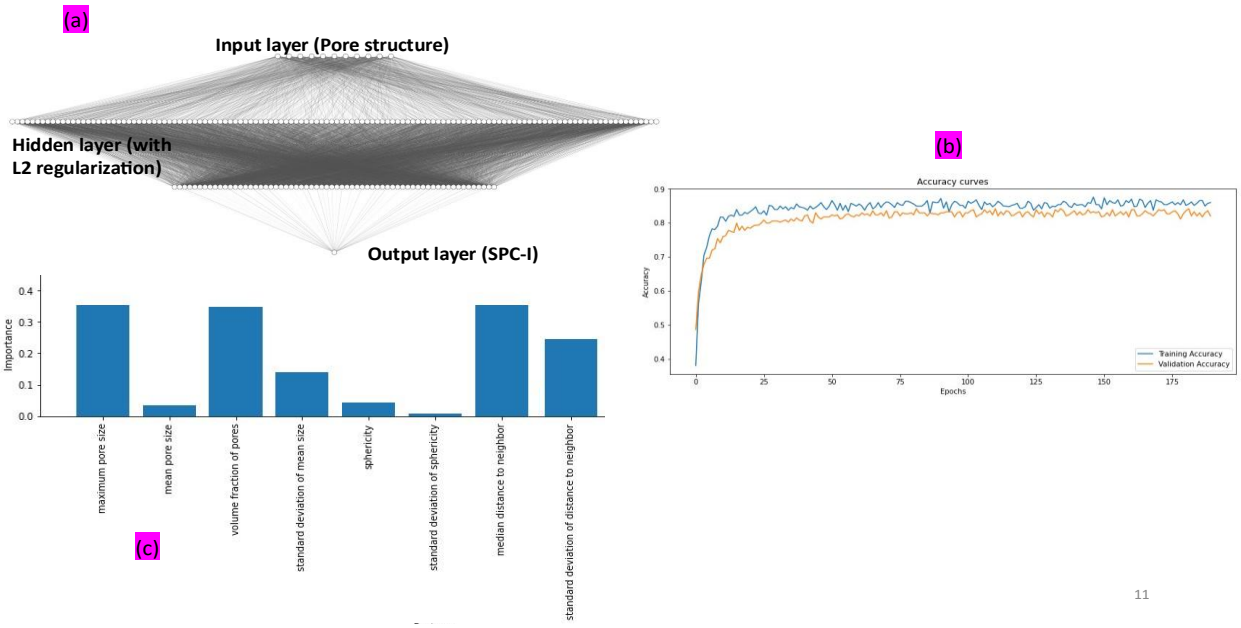

Figure 12. DNN-based validation using the full augmented dataset: (a) schematic illustration of the DNN model used; (b) accuracy plot for the DNN training; (c) feature importance predicted by the training in (b).

4. Discussion

4.1 Physical Interpretation of Clustered Porosity Evolution

The clustering framework revealed a progressive transition from isolated pore behavior toward interaction-dominated porosity networks. The dominance of size-related descriptors in the PCA space is physically significant because nonlinear acoustic behavior is strongly influenced by defect geometry, local stress concentration, and distributed nonlinear interaction mechanisms [13–16]. Larger pores and broader pore-size distributions increase localized stress amplification and nonlinear scattering behavior, thereby enhancing spectral sideband generation and SPC-I sensitivity. Similarly, structure irregularity and distributed defect interaction contribute to nonlinear modulation effects and cumulative acoustic nonlinearity.

As described in Table 8, Cluster 3 corresponds to small, near-spherical, and spatially uniform pores that generate a comparatively weak acoustic response. In this regime, SPC-I is governed primarily by isolated pore features such as pore size and volume fraction. Cluster 2 represents a transitional state characterized by increasing pore growth, increasing variability, and the onset of clustering-induced pore interactions. In this regime, localized stress concentration and nonlinear modulation effects become increasingly significant. Cluster 1 corresponds to severe porosity characterized by large, irregular, and spatially clustered defects. In this regime, the hybrid ultrasonic response becomes strongly interaction-dominated due to enhanced defect-network behavior, local contact acoustic nonlinearity, and distributed nonlinear scattering. The monotonic increase in SPC-I across these regimes supports the interpretation that SPC-I reflects more cumulative acoustic interaction

between nearby pores rather than simply total defect quantity, when the size or the volume fraction of the pores exceeds a threshold [13–21,23].

4.2 Engineering Implications of the SPC-I–PI Framework

The combined SPC-I–PI methodology provides a practical framework for porosity-sensitive material characterization in additively manufactured IN718. The results indicate that SPC-I can serve as:

1. A rapid screening indicator for porosity severity,
2. A defect-sensitive nonlinear structural health monitoring metric,
3. A rapid screening indicator of evolving microstructural state.

Importantly, the clustering analysis demonstrates that SPC-I does not merely correlate with porosity quantity but reflects evolving defect interaction regimes and nonlinear material behavior. This capability is particularly valuable for scalable inspection and quality-control workflows in additive manufacturing, where full XCT characterization of every component is often impractical [6–10]. PI is not intended to replace XCT or to predict SPC-I. PI is intended to fuse acoustic and XCT information into an interpretable descriptor.

4.3 Limitations and Future Research

Several assumptions should be considered when interpreting the present findings. First, the small experimental dataset limits statistical generalization and reduces the robustness of regression, clustering, and machine-learning analyses. Although consistent trends were observed across the SPC-I, PI, PCA, and clustering frameworks, additional specimens spanning broader porosity distributions and manufacturing conditions will be necessary to establish stronger statistical confidence and improve model generalizability.

Second, the XCT-derived descriptors are influenced by factors such as voxel resolution, segmentation threshold selection, and surface reconstruction methodology. These factors can introduce uncertainty into pore structure measurements, particularly for small or irregularly shaped defects. Because the proposed PI framework relies directly on XCT-derived structure-sensitive descriptors, uncertainties in image processing may propagate into the regression and clustering analyses [6–10,32–34]

On the nonlinear ultrasonic side, SPC-I sensitivity depends on experimental and signal-processing parameters, including excitation conditions, threshold selection, spectral windowing, and peak-detection criteria [18]. Furthermore, the present study employed a primarily single-direction nonlinear ultrasonic configuration and therefore did not explicitly evaluate anisotropic effects associated with build orientation and directional microstructural evolution in additively manufactured materials. Consequently, the current SPC-I framework should be interpreted as an initial structure-sensitive screening methodology rather than a fully generalized nonlinear characterization framework [27–29].

Undeniably, highlighting the benefit of showing PI is an effective tool to overcome the present challenges to employ SPC for quantitative assessment. Future studies will focus on refining the physics-informed Porosity Index (PI) formulation through feature-selection optimization, sensitivity analysis, and physics-guided weighting strategies. Combining advanced XCT-derived structure descriptors with validated machine-learning workflows and multimodal characterization techniques may further improve porosity-state classification and hybrid response prediction.

Finally, although the present work focused on additively manufactured IN718, the proposed XCT–SPC-I–PI framework may also have broader applicability to other AM alloys and potentially to infrastructure materials and structural systems in which distributed defect populations, microstructural heterogeneity, and nonlinear interaction mechanisms govern structural performance.

5. Conclusions

This study investigated the relationship between hybrid ultrasonic response and porosity characteristics in additively manufactured Inconel 718 by integrating XCT-derived porosity descriptors with the Sideband Peak Count Index (SPC-I). The results demonstrated that SPC-I is sensitive not only to porosity volume fraction but also to pore structure, pore size variability, spatial organization, and defect interaction mechanisms. Stronger correlations were observed for descriptors associated with pore size evolution and structure than for pore-spacing metrics alone. To improve the interpretation of hybrid acoustic behavior, a physics-informed Porosity Index (PI) framework was proposed. By combining normalized XCT-derived descriptors with SPC-I, the PI provided a structure-sensitive data-fusion framework that facilitated the interpretation of SPC-I porosity relationships by integrating XCT-derived descriptors with acoustic measurements. This study represents the first implementation of an integrated XCT–SPC-I–PI framework for porosity characterization in additively manufactured IN718.

PCA and clustering analyses revealed three structure-dependent porosity regimes. Statistical testing confirmed significant differences between the low-porosity regime (Cluster 3) and the higher-porosity regimes (Clusters 1 and 2), indicating a transition toward interaction-dominated defect networks. Furthermore, cluster-wise regression produced stronger correlations than global regression, demonstrating that the hybrid ultrasonic response is governed by evolving defect interaction mechanisms rather than a single universal porosity-response relationship.

Overall, the proposed XCT–SPC-I–PI framework provides a physically interpretable and scalable approach for rapid porosity-sensitive characterization of additively manufactured materials. The results support the use of SPC-I as a rapid screening indicator of porosity state and acoustic response, offering potential applications in nondestructive evaluation, quality assurance, and structural health monitoring of AM components. The proposed framework establishes a pathway toward rapid hybrid ultrasonic qualification of additively manufactured components, where SPC-I provides scalable screening while XCT-based calibration supports interpretation during process qualification.

References

[1] A. Mostafaei, R. Ghiaasiaan, I.T. Ho, S. Strayer, K.C. Chang, N. Shamsaei, S. Shao, S. Paul, A.C. Yeh, S. Tin, A.C. To, Additive manufacturing of nickel-based superalloys: A state-of-the-art review on process-structure-defect-property relationship, Prog. Mater. Sci. 136 (2023). https://doi.org/10.1016/j.pmatsci.2023.101108.

[2] M. Tang, P.C. Pistorius, J.L. Beuth, Prediction of lack-of-fusion porosity for powder bed fusion, Addit. Manuf. 14 (2017). https://doi.org/10.1016/j.addma.2016.12.001.

[3] M.L. Wang, X.G. Yang, B. Li, D.Q. Shi, G.L. Miao, S.Q. Guo, Y.S. Fan, The dominant role of defects on fatigue behaviour of a SLM Ni-based superalloy at elevated temperature, Int. J. Fatigue 176 (2023). https://doi.org/10.1016/j.ijfatigue.2023.107894.

[4] M.S. Dodaran, M. Muhammad, N. Shamsaei, S. Shao, Synergistic effect of microstructure and defects on the initiation of fatigue cracks in additively manufactured Inconel 718, Int. J. Fatigue 162 (2022). https://doi.org/10.1016/j.ijfatigue.2022.107002.

[5] H. Gong, K. Rafi, H. Gu, T. Starr, B. Stucker, Analysis of defect generation in Ti-6Al-4V parts made using powder bed fusion additive manufacturing processes, Addit. Manuf. 1 (2014). https://doi.org/10.1016/j.addma.2014.08.002.

[6] I.T. Ho, K. Muralidharan, S. Tin, D. Bayly, B. Gockel, M. Reale, T. Kundu, Non-destructive evaluation of additively manufactured superalloy IN718 via integrating microfocus X-ray computed tomography and non-linear acoustics, Addit. Manuf. 96 (2024). https://doi.org/10.1016/j.addma.2024.104539.

[7] A. Du Plessis, S.G. Le Roux, J. Els, G. Booysen, D.C. Blaine, Application of microCT to the non-destructive testing of an additive manufactured titanium component, Case Studies in Nondestructive Testing and Evaluation 4 (2015). https://doi.org/10.1016/j.csndt.2015.09.001.

[8] F.H. Kim, H. Yeung, E.J. Garboczi, Characterizing the effects of laser control in laser powder bed fusion on near-surface pore formation via combined analysis of in-situ melt pool monitoring and X-ray computed tomography☆, Addit. Manuf. 48 (2021). https://doi.org/10.1016/j.addma.2021.102372.

[9] J. Elambasseril, S.L. Lu, Y.P. Ning, N. Liu, J. Wang, M. Brandt, H.P. Tang, M. Qian, 3D characterization of defects in deep-powder-bed manufactured Ti–6Al–4V and their influence on tensile properties, Materials Science and Engineering: A 761 (2019). https://doi.org/10.1016/j.msea.2019.138031.

[10] R. Snell, S. Tammas-Williams, L. Chechik, A. Lyle, E. Hernández-Nava, C. Boig, G. Panoutsos, I. Todd, Methods for Rapid Pore Classification in Metal Additive Manufacturing, JOM 72 (2020). https://doi.org/10.1007/s11837-019-03761-9.

[11] C. Bermes, J.Y. Kim, J. Qu, L.J. Jacobs, Nonlinear Lamb waves for the detection of material nonlinearity, Mech. Syst. Signal Process. 22 (2008). https://doi.org/10.1016/j.ymssp.2007.09.006.

[12] J. Segers, S. Hedayatrasa, G. Poelman, W. Van Paepegem, M. Kersemans, Broadband nonlinear elastic wave modulation spectroscopy for damage detection in composites, Struct. Health Monit. 21 (2022). https://doi.org/10.1177/14759217211002562.

[13] Y. Zheng, R.G. Maev, I.Y. Solodov, Nonlinear acoustic applications for material characterization: A review, Can. J. Phys. 77 (1999). https://doi.org/10.1139/cjp-77-12-927.

[14] Y. Li, S. Hu, C.H. Henager, Microstructure-based model of nonlinear ultrasonic response in materials with distributed defects, J. Appl. Phys. 125 (2019). https://doi.org/10.1063/1.5083957.

[15] T. Kundu, Nonlinear ultrasonic and Vibro-acoustical techniques for Nondestructive evaluation, 2018. https://doi.org/10.1007/978-3-319-94476-0.

[16] C. Pecorari, I. Solodov, Nonclassical Nonlinear Dynamics of Solid Surfaces in Partial Contact for NDE Applications, in: Universality of Nonclassical Nonlinearity, 2006. https://doi.org/10.1007/978-0-387-35851-2_19.

[17] G. Zhang, M. Wang, O. Achouham, U. Amjad, H. Alnuaimi, C. Mechri, R.E. Guerjouma, T. Kundu, Validating sideband peak count-index (SPC-I) technique as a hybrid linear/nonlinear ultrasonic technique through numerical modeling and experiment, Ultrasonics 162 (2026). https://doi.org/10.1016/j.ultras.2026.107966.

[18] S.H. Park, I. Bokhari, H. Alnuaimi, U. Amjad, R. Fleischman, T. Kundu, Early detection of steel tube welded joint failure using SPC-I nonlinear ultrasonic technique, Struct. Health Monit. 24 (2025). https://doi.org/10.1177/14759217241235057.

[19] S.H. Park, T. Kundu, A modified sideband peak count based nonlinear ultrasonic technique for material characterization, Ultrasonics 128 (2023). https://doi.org/10.1016/j.ultras.2022.106858.

[20] G. Zhang, X. Li, S. Zhang, T. Kundu, Sideband peak count-index technique for monitoring multiple cracks in plate structures using ordinary state-based peri-ultrasound theory, J. Acoust. Soc. Am. 152 (2022). https://doi.org/10.1121/10.0015242.

[21] G. Zhang, X. Li, T. Li, T. Kundu, Ordinary state-based peri-ultrasound modeling for monitoring crack propagation in plate structures using sideband peak count-index technique, J. Sound Vib. 568 (2024). https://doi.org/10.1016/j.jsv.2023.117962.

[22] P. Liu, H. Sohn, Damage detection using sideband peak count in spectral correlation domain, J. Sound Vib. 411 (2017). https://doi.org/10.1016/j.jsv.2017.08.049.

[23] G. Zhang, B. Hu, H. Alnuaimi, U. Amjad, T. Kundu, Numerical modeling with experimental verification investigating the effect of various nonlinearities on the sideband peak count-index technique, Ultrasonics 138 (2024). https://doi.org/10.1016/j.ultras.2024.107259.

[24] S.H. Park, H. Alnuaimi, A. Hayes, M. Sitkiewicz, U. Amjad, K. Muralidharan, T. Kundu, Nonlinear Acoustic Technique for Monitoring Porosity in Additively Manufactured Parts, J. Nondestruct. Eval. Diagn. Progn. Eng. Syst. 5 (2022). https://doi.org/10.1115/1.4053252.

[25] P. Liu, L. Yang, K. Yi, T. Kundu, H. Sohn, Application of nonlinear ultrasonic analysis for in situ monitoring of metal additive manufacturing, Struct. Health Monit. 22 (2023). https://doi.org/10.1177/14759217221113447.

[26] M.H. Hafezi, R. Alebrahim, T. Kundu, Peri-ultrasound for modeling linear and nonlinear ultrasonic response, Ultrasonics 80 (2017). https://doi.org/10.1016/j.ultras.2017.04.015.

[27] D. Chopra, R. Khurana, Introduction to Machine Learning with Python, 2023. https://doi.org/10.2174/9789815124422123010l.

[28] G. James, D. Witten, T. Hastie, R. Tibshirani, An Introduction to Statistical Learning Second Edition, Springer Texts 102 (2023).

[29] A. Maugeri, M. Barchitta, G. Favara, C. La Mastra, M.C. La Rosa, R. Magnano San Lio, A. Agodi, The Application of Clustering on Principal Components for Nutritional Epidemiology: A Workflow to Derive Dietary Patterns, Nutrients 15 (2023). https://doi.org/10.3390/nu15010195.

[30] Paraview-5.11, (n.d.). https://www.paraview.org/.

[31] J. Ahrens, B. Geveci, C. Law, ParaView: An end-user tool for large-data visualization, in: Visualization Handbook, 2005. https://doi.org/10.1016/B978-012387582-2/50038-1.

[32] C. Portaneri, M. Rouxel-Labbé, M. Hemmer, D. Cohen-Steiner, P. Alliez, Alpha wrapping with an offset, ACM Trans. Graph. 41 (2022). https://doi.org/10.1145/3528223.3530152.

[33] E. Fogel, M. Teillaud, The Computational Geometry Algorithms Library CGAL, ACM Communications in Computer Algebra 49 (2015). https://doi.org/10.1145/2768577.2768579.

[34] H. Wadell, Volume, Shape, and Roundness of Quartz Particles, J. Geol. 43 (1935). https://doi.org/10.1086/624298.

[35] J. Ye, A. Poudel, J. (Peter) Liu, A. Vinel, D. Silva, S. Shao, N. Shamsaei, Machine learning augmented X-ray computed tomography features for volumetric defect classification in laser beam powder bed fusion, International Journal of Advanced Manufacturing Technology 126 (2023). https://doi.org/10.1007/s00170-023-11281-9.